Cell

Structure-guided discovery of bile acid derivatives for treating liver diseases without causing itch

Graphical abstract

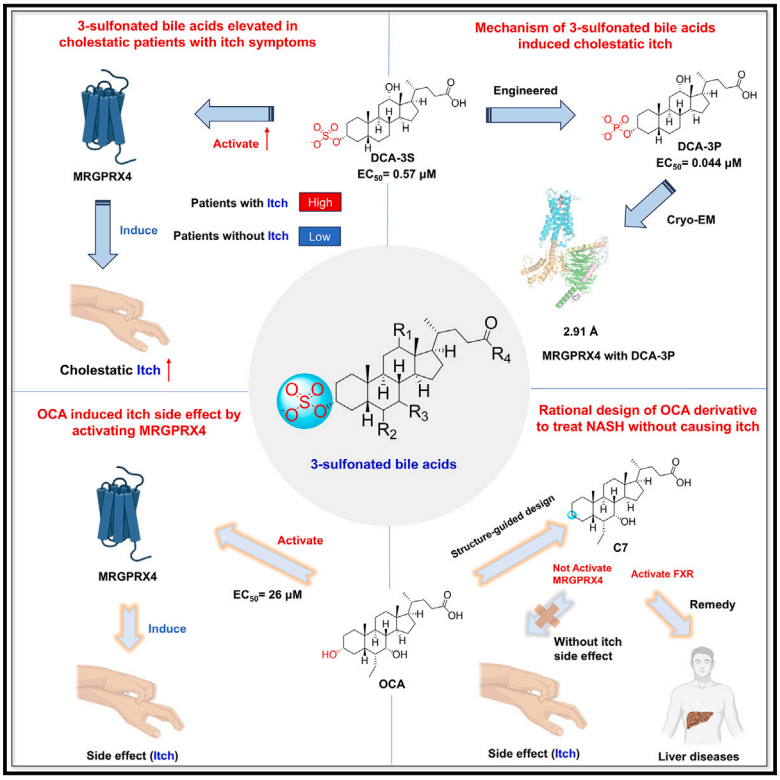

Highlights

- 3-sulfated bile acids accumulate in cholestatic patients, causing itch symptoms
- The cryo-EM structure of MRGPRX4 (hX4) with DCA-3P unveils how bile acids activate hX4
- Obeticholic acid (OCA) induces an itch side effect by activating hX4
- An OCA derivative, C7, was developed to treat liver diseases without causing itch

Authors

Jun Yang, Tianjun Zhao, Junping Fan, ..., Yu Chen, Yulong Li, Xiaoguang Lei

Correspondence

chybeyond1071@ccmu.edu.cn (Y.C.), yulongli@pku.edu.cn (Y.L.), xglei@pku.edu.cn (X.L.)

In brief

Bile acids (BAs) are 3-sulfonated to improve their potency to activate MRGPRX4 (hX4), the G-protein-coupled receptor for cholestatic itch. The cryo-EM structure of hX4 binding with a bile acid-derived agonist highlights the importance of the 3-hydroxyl group in BAs to activate hX4 and helps develop the lead compound, C7, as a promising candidate for treating liver diseases without the unwanted side effect of itch.

Yang et al., 2024, Cell *187*, 1–19
December 12, 2024
https://doi.org/10.1016/j.cell.2024.10.001

CellPress

Cell

CellPress

Article

Structure-guided discovery of bile acid derivatives for treating liver diseases without causing itch

Jun Yang,[1,2,9] Tianjun Zhao,[2,3,4,9] Junping Fan,[1,9] Huaibin Zou,[5,9] Guangyi Lan,[3,4] Fusheng Guo,[1,2] Yaocheng Shi,[1] Han Ke,[1] Huasheng Yu,[6] Zongwei Yue,[1,2] Xin Wang,[1,7] Yingjie Bai,[1,7] Shuai Li,[8] Yingjun Liu,[8] Xiaoming Wang,[8] Yu Chen,[5,*] Yulong Li,[2,3,4,*] and Xiaoguang Lei[1,2,7,10,*]

[1]Beijing National Laboratory for Molecular Sciences, Key Laboratory of Bioorganic Chemistry and Molecular Engineering of Ministry of Education, College of Chemistry and Molecular Engineering, Peking University, Beijing 100871, China
[2]Peking-Tsinghua Center for Life Sciences, Academy for Advanced Interdisciplinary Studies, Peking University, Beijing 100871, China
[3]State Key Laboratory of Membrane Biology, School of Life Sciences, Peking University, Beijing 100871, China
[4]PKU-IDG/McGovern Institute for Brain Research, New Cornerstone Science Laboratory, Beijing 100871, China
[5]Fourth Department of Liver Disease, Beijing Youan Hospital, Capital Medical University, Beijing 100069, China
[6]Department of Neuroscience, Perelman School of Medicine, University of Pennsylvania, Philadelphia, PA 19104, USA
[7]Institute for Cancer Research, Shenzhen Bay Laboratory, Shenzhen 518107, China
[8]Hepaitech (Beijing) Biopharma Technology Co., Ltd., Beijing, China
[9]These authors contributed equally
[10]Lead contact
*Correspondence: chybeyond1071@ccmu.edu.cn (Y.C.), yulongli@pku.edu.cn (Y.L.), xglei@pku.edu.cn (X.L.)
https://doi.org/10.1016/j.cell.2024.10.001

SUMMARY

Chronic itch is a debilitating symptom profoundly impacting the quality of life in patients with liver diseases like cholestasis. Activation of the human G-protein coupled receptor, MRGPRX4 (hX4), by bile acids (BAs) is implicated in promoting cholestasis itch. However, the detailed underlying mechanisms remain elusive. Here, we identified 3-sulfated BAs that are elevated in cholestatic patients with itch symptoms. We solved the cryo-EM structure of hX4-Gq in a complex with 3-phosphated deoxycholic acid (DCA-3P), a mimic of the endogenous 3-sulfated deoxycholic acid (DCA-3S). This structure revealed an unprecedented ligand-binding pocket in MRGPR family proteins, highlighting the crucial role of the 3-hydroxyl (3-OH) group on BAs in activating hX4. Guided by this structural information, we designed and developed compound 7 (C7), a BA derivative lacking the 3-OH. Notably, C7 effectively alleviates hepatic injury and fibrosis in liver disease models while significantly mitigating the itch side effects.

INTRODUCTION

Non-alcoholic fatty liver disease (NAFLD) is the most common form of chronic liver disease worldwide, with a global prevalence of around 25%, affecting over half of patients with type 2 diabetes.[1,2] Furthermore, nearly one-third of the patients with NAFLD progress to non-alcoholic steatohepatitis (NASH), characterized by hepatic steatosis, inflammation, and fibrosis, which can ultimately culminate in liver cirrhosis and hepatocellular carcinoma, with liver transplantation as the sole viable treatment option.[3] Despite NASH surpassing hepatitis C as the leading cause of liver transplantation,[4,5] there are currently no FDA-approved drugs available for its treatment.

The farnesoid X receptor (FXR), a nuclear receptor of BAs,[6–8] plays a pivotal role in regulating the hepatic bile acid (BA)'s levels,[9–12] controlling *de novo* lipogenesis, mediating lipid absorption,[13] and regulating the expression of genes related to glucose regulation,[14,15] autophagy,[16,17] and inflammation.[18,19] This multifaceted functionality has brought FXR into the spotlight, garnering considerable attention for novel therapeutic compounds for liver diseases, including NASH.[20]

Obeticholic acid (OCA), a semi-synthetic BA derivative, is a "first-in-class" FXR agonist with a nearly 100-fold higher affinity for FXR than its parent compound, chenodeoxycholic acid (CDCA).[21] OCA has been approved to treat primary biliary cholangitis (PBC) and hepatic and metabolic diseases.[22–24] However, clinical trials showed that OCA could significantly increase low-density lipoprotein cholesterol (LDL-C) levels and the incidence of pruritus.[22–31] Notably, pruritus is by far the most common OCA-associated adverse effect, and it is dose-dependent, sometimes necessitating discontinuation of the trial for certain patients. Although the concomitant use of statins can attenuate the increase in LDL-C levels,[32,33] the mechanism underlying OCA-induced pruritus remains unclear.

Please cite this article in press as: Yang et al., Structure-guided discovery of bile acid derivatives for treating liver diseases without causing itch, Cell (2024), https://doi.org/10.1016/j.cell.2024.10.001

BAs are the end products of cholesterol metabolism in the liver and play an essential role in many physiological activities.[34–38] Cholestasis, caused by several different genetic, hormonal, pharmacologic, or physical cues, often leads to the accumulation of BAs.[39–41] One of the most common symptoms of cholestasis is pruritus, or chronic itch, affecting up to 80% of patients suffering from hepatocellular and cholangiocellular cholestasis. This agonizing itch often leads to severe sleep deprivation, depression, and even suicidal thoughts, significantly reducing the life quality of patients.[42–44] Current therapeutic approaches for cholestatic pruritus (CP), including rifampicin,[45] ursodeoxycholic acid (UDCA),[46] cholestyramine,[47] and bezafibrate,[48] only showed limited efficacy for reducing the itch symptoms of patients with cholestasis and were often accompanied by side effects. Till now, limited effective drugs have been developed to treat CP due to the unclear itching mechanisms.

Many clinical studies have suggested the close association between BAs and CP.[49–51] Importantly, human MRGPRX4 (hX4), a G protein-coupled receptor expressed in human dorsal root ganglion (DRG) neurons,[52–54] was recently reported as an endogenous receptor for CP.[52,55] The lack of detailed mechanistic insights significantly hindered the clinic's diagnosis and treatment of CP.

Herein, we identified that cholestatic patients with itching symptoms have accumulated 3-sulfated BAs compared with those without itching. This sulfation increases BA's affinity to hX4, aggravating BA-induced itch symptoms in hX4 humanized rats. Furthermore, using a more potent agonist of hX4, 3-phosphated deoxycholic acid (DCA-3P), we solved the cryoelectron microscopy (cryo-EM) structure of DCA-3P-bounded hX4 and unveiled the vital role of BA' 3-hydroxyl group (3-OH) group in activating hX4. Moreover, we confirmed that OCA induces itch side effects by activating hX4. Based on the structural insight into how BAs activate hX4, we developed C7, a derivative of OCA without 3-OH. C7 shows high potency in activating human FXR but not hX4. Accordingly, C7 does not induce pruritus in humanized rats, making it a promising new drug candidate for treating liver diseases without the unwanted side effects of itch.

RESULTS

Elevated 3-sulfated BAs are positively associated with cholestatic itch

Previous studies have revealed that BAs are related to CP by activating hX4[52,55] (Figure 1A). To understand which specific BAs are more critical in inducing itching, plasma samples were collected from cholestatic patients with obvious itch symptoms (itch, n = 14) and without itch symptoms (non-itch, n = 20). 28 types of BAs were analyzed using liquid chromatography-tandem mass spectrometry (LC-MS/MS) (Figure 1B; Data S1). Although the concentration of total BAs in itch patients was considerably higher than that in non-itch patients (p = 0.034 < 0.05) (Figure 1C), most individual BAs had no significant difference between itch and non-itch groups except for TCDCA, GUDCA, and some specific 3-sulfated BAs, such as GUDCA-3S, TUDCA-3S, and TCDCA-3S (Figures S1A–S1E; Data S1). Interestingly, the concentration of total 3-sulfated BAs (BAs-3S) in itch patients was significantly higher than non-itch (p = 0.002 < 0.01), suggesting that 3-sulfated BAs may play a more critical role in CP (Figure 1D; Data S1). Additionally, previous studies have revealed that sulfated BA levels are elevated in patients with liver diseases,[56,57] particularly in cholestatic patients.[50,58] The sulfation of BAs at 3-OH, catalyzed by sulfotransferase-2A1 (SULT2A1) in the liver, is a prevalent modification of BAs in humans for detoxification due to the higher solubility of sulfonated products[59] (Figure 1E). A recent study also uncovered that enzymes from intestinal flora can sulfate the 3-OH of BAs.[60] Some clinical cases also implied the relationship between the sulfation of BAs and CP.[45,61] Therefore, all the above results suggested that 3-sulfated BAs accumulate in cholestatic patients with pruritus, and these 3-sulfated BAs may promote pruritus symptoms.

3-sulfated BAs show higher potency to activate hX4 than other BAs do

Because hX4 is the receptor of BAs and is closely associated with cholestatic itch,[52,55] we envisioned that 3-sulfonation modification of BAs promotes pruritus by improving the potency to activate hX4. To understand the relationship between modifications of BAs and their affinity to hX4, we initially determined the activity of 30 different BAs toward hX4 using the FLIPR-Ca^{2+} assay. hX4 could be activated by most of the BAs with varying potency, and among all the tested BAs, DCA and UDCA exhibited higher activity potency than CA, CDCA, and LCA (Figure 1F). Additionally, the conjugation of the carboxyl group of BAs with glycine or taurine significantly reduced their activity. Interestingly, we also discovered that different modifications of 3-OH in BAs impacted the degree of activation toward hX4. The activity was negatively affected by the oxidation of the 3-OH group to the carbonyl group (such as 3-oxo-DCA, 3-oxo-LCA, and 3-oxo-CA), while sulfonation of this group significantly enhanced the activity (Figure 1F). Moreover, sulfated products of DCA, CA, LCA, GUDCA, and TUDCA exhibit lower EC_{50}, suggesting a positive effect of 3-sulfated on activating hX4 (Figures 1G and S1F–S1I). To further confirm whether the concentration of 3-OH sulfated BAs in the plasma of cholestatic patients can activate hX4, we prepared artificial 3-sulfated BA mixtures according to the concentration of those BAs in patients with itch (itch mix) and patients without itch (non-itch mix) and determined the activation of these mixtures toward hX4. Interestingly, both the mixtures can activate hX4, and the itch mix can induce a higher signal than the non-itch mix, while no signal was detected when using 1× itch mix to activate non-transduced parental cells (Figure 1H). All these results demonstrated that pathologically relevant levels of 3-sulfated BAs are sufficient to activate hX4. Due to DCA and its 3-sulfonated product (DCA-3S) showing the highest activity toward hX4, we selected these two BAs to further study their activating mechanism.

DCA-3S promotes more severe itch behavior than DCA does in the hX4-humanized rat model

Due to hX4 only expressing in human itch-related DRG neurons, not in mice or rats,[52] it is impossible to conduct animal behavioral experiments directly to confirm whether DCA-3S can exacerbate itch behavior by activating hX4. Despite the shared characteristics among species about receptors, neural types, and itch

Please cite this article in press as: Yang et al., Structure-guided discovery of bile acid derivatives for treating liver diseases without causing itch, Cell (2024), https://doi.org/10.1016/j.cell.2024.10.001

CellPress

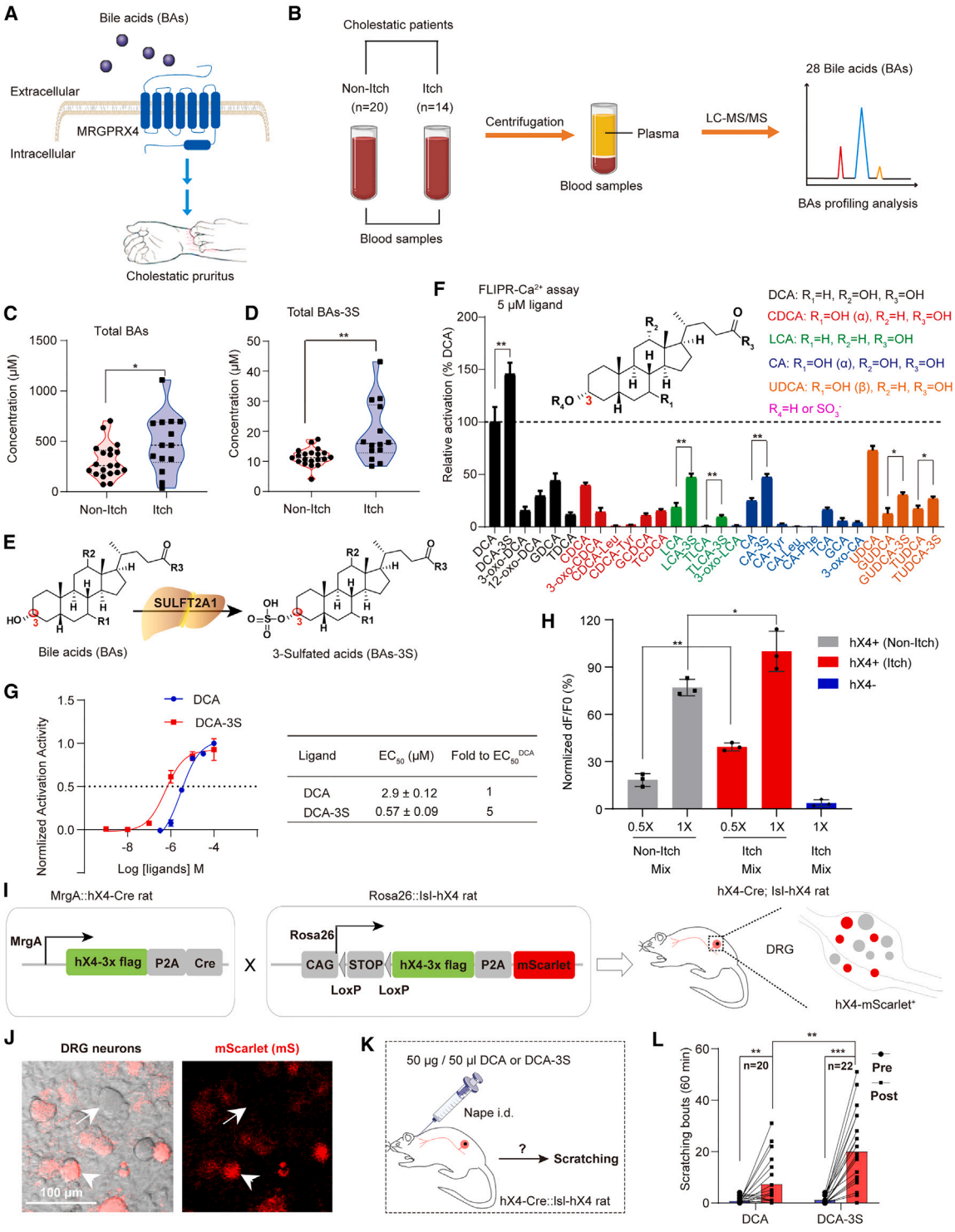

Figure 1. 3-sulfated BAs promote chronic itch in cholestatic patients through activating hX4

(A) BAs can activate hX4 and are related to cholestatic pruritus.

(B) LC-MS/MS was utilized to analyze BA profiling in cholestatic patients' plasma.

(C and D) Total BAs (C) and 3-OH sulfated BAs (D) content elevate in patients' plasma with itch symptoms.

(E) To detoxify BAs, they can be transformed into BAs-3S by SULFT2A1 in the liver.

(F) Relative activation activity of 5 μM different BAs toward hX4 using FLIPR-Ca^{2+} assay. R1–R4 represents different modifications in these positions.

(G) EC_{50} determination of DCA and DCA-3S toward hX4 using FLIPR-Ca^{2+} assay.

(legend continued on next page)

signaling pathways, differences also exist in the cellular basis and neuronal coding of pruriception.[62,63] To solve the problem, initially, DCA was intradermally injected into the nape of mice's or rats' necks (Figures S2A and S2B), and we found that intradermal injection of DCA induced significant scratching in mice but not in rats (Figures S2C and S2D), reflecting the inter-species difference. Therefore, rats were chosen to generate an hX4 humanized animal model for itch behavioral experiments to eliminate the false-positive results.

MrgA (*MrgA3* in mice) is a known itch receptor, which is expressed in a subset of itch-related neurons in rat DRG neurons[64] and mediates chloroquine (CQ)-induced itch in both rats and mice[65] (Figures S2C and S2D). To express hX4 in rat itch-related DRG neurons, we replaced the coding sequence of the *MrgA* gene in rat with *hX4-3x flag-P2A-Cre* to generate the *MrgA::hX4-Cre* rat (*hX4-Cre* rat), which expresses Cre recombinase under the control of the *MrgA* promotor (Figure 1I). We also generated the *Rosa26::loxp-STOP-loxp-hX4-3x flag-mScarlet* (mS) rat (*lsl-hX4* rat), in which the expression of hX4 is Cre recombinase dependent (Figure 1I). Offspring generated from crossing these two lines (*hX4-cre; lsl-hX4* rat) that inherit both *hX4-Cre* and *lsl-hX4* will express hX4 selectively in *MrgA* lineage neurons, indicated by red fluorescent protein mS (Figure 1J). Additionally, we confirmed the expression of hX4 in rat DRG neurons by showing the co-localization of the hX4 antibody and FLAG antibody immunostaining signals with mS (Figure S2E). Subsequently, we tested whether DCA induces itch in *hX4-cre; lsl-hX4* rat model (Figure S2F). We found that intradermal injection of DCA into the nape of their neck triggered significant scratching behavior in *hX4-cre; lsl-hX4* rats but not in littermate controls or wild-type (WT) rats (Figure S2G).

Subsequently, to test whether DCA-3S can induce more severe itch in the humanized rat model, we intradermally injected DCA or DCA-3S into the nape of *hX4-cre; lsl-hX4* rats' necks and recorded their scratching behavior before and after injection for 60 min (Figure 1K). There was a significant increase in scratching bouts after injection of DCA or DCA-3S, and the scratching frequency was significantly higher in rats injected with DCA-3S than those with DCA (Figure 1L). These results suggest that DCA and DCA-3S could induce itch symptoms by activating hX4, and 3-sulfated DCA exacerbates the itch symptom, probably owing to its higher affinity.

The cryo-EM structure of hX4 reveals its binding with a BA-like agonist, DCA-3P

To understand the mechanism of BAs activating hX4 and sulfonation of 3-OH enhancing the activity, we tried to resolve the structure of hX4 bound with DCA-3S. Although we have tried many strategies using cryo-EM, no apparent density map of the ligand was found in the binding pocket. Recently, the structure of hX4 bound to the exogenous agonist MS47134 ($X4^{MS47134}$) was solved using cryo-EM, and the ligand-binding pocket of hX4 is rich in positively charged amino acids.[66,67] Therefore, it seems reasonable that sulfonation of DCA could enhance its affinity for the receptor because sulfonate carries one negative charge (Figure 2A). Based on these, we speculated that modification of 3-OH with a group carrying more negative charges could further enhance the activity of BAs to hX4. We synthesized an unnatural BA DCA-3P with a phosphate group modification on 3-OH (Figure 2A). As expected, DCA-3P shows a 65-fold and 13-fold higher activity for hX4 than DCA and DCA-3S, respectively, with an EC_{50} of 44 nM (Figure 2B). Similarly, another potent synthetic and non-BA hX4 agonist with phosphate modification, PSB-22034, was recently reported.[68]

We solved the cryo-EM complex structure of hX4 with DCA-3P at a resolution of 2.91 Å (Figures 2C and 2D; Data S2). The electron microscopy density of the structure enables us to build most residues of the complex and confidently fit DCA-3P into the map (Data S2). DCA-3P consists of three crucial parts: a phosphate group head (P-head), an intermediate hydrophobic region (H-middle), and a carboxyl tail (C-tail) (Figure 2E). Compared with $X4^{MS47134}$, the overall structure of DCA-3P-bound hX4 ($X4^{DCA-3P}$) resembles the reported structure at the intracellular side, while the extracellular side of $X4^{DCA-3P}$ has significant conformation changes (Figure 2F; Data S2). Specifically, TM2, TM3, ECL1, and ECL3 displaced 6.3, 2.9, 4.3, and 7.1 Å inward, respectively, resulting in a narrow binding pocket for the P-head of DCA-3P; however, in the structure of $X4^{MS47134}$, those regions flipped outward, providing enough space to accommodate the phenyl group of MS47134 (Figure 2F).

BAs occupy the orthostatic binding pocket of hX4

Interestingly, the binding pocket occupied by DCA-3P in hX4 completely differs from agonists in other reported MRGPRs (Figure 2G; Data S2). Unlike MS47134, which lies flat on the extracellular side of hX4 and near the surface, DCA-3P inserts vertically into the orthostatic binding site (Figure 2G). Specifically, the C-tail of DCA-3P extends to a space composed of TM3, TM4, TM5, and TM6, and the H-middle is surrounded by TM3, TM6, and TM7. P-head occupies a similar position to MS47134, surrounded by TM1, TM2, and TM3 (Data S2). It is worth mentioning that DCA-3P is the first agonist discovered binding into the canonical pocket in MRGPR family receptors. In the reported structures, agonists in both MRGPRX1[69,70] and MRGPRX2[66,71] bind close to the surface of the extracellular side, while DCA-3P extends deeper toward the $G229^{6.48}$ (Data S2). Similar to agonist

(H) Activation of hX4 in HEK293T cells induced by application of a mixture of artificial 3-OH sulfated BAs derived from cholestatic patients with itch (itch mix) and patients without itch (non-itch mix). "hX4+" and "hX4−" represent HEK293T cells transfected with hX4 and non-transduced parental cells, respectively. The results were determined using FLIPR-Ca^{2+} assay and normalized to the signal measured using 1× itch mix. $n = 3$ per group.

(I) Scheme of the strategy used to generate hX4 humanized rats.

(J) Brightfield (BF) and mScarlet (mS) images of cultured DRG neurons isolated from a humanized rat. The arrow and arrowhead indicate mS-negative and mS-positive neurons, respectively.

(K) DCA or DCA-3S was injected into the nape of the humanized rats, and scratching behavior was recorded for 60 min.

(L) DCA and DCA-3S can significantly induce itch symptoms when injected into rats. $n = 20–22$ per group.

For all panels, data are represented as mean ± SEM; Student's t test, * "$p < 0.05$," ** "$p < 0.01$," *** "$p < 0.001$."

See also Figures S1 and S2 and Data S1.

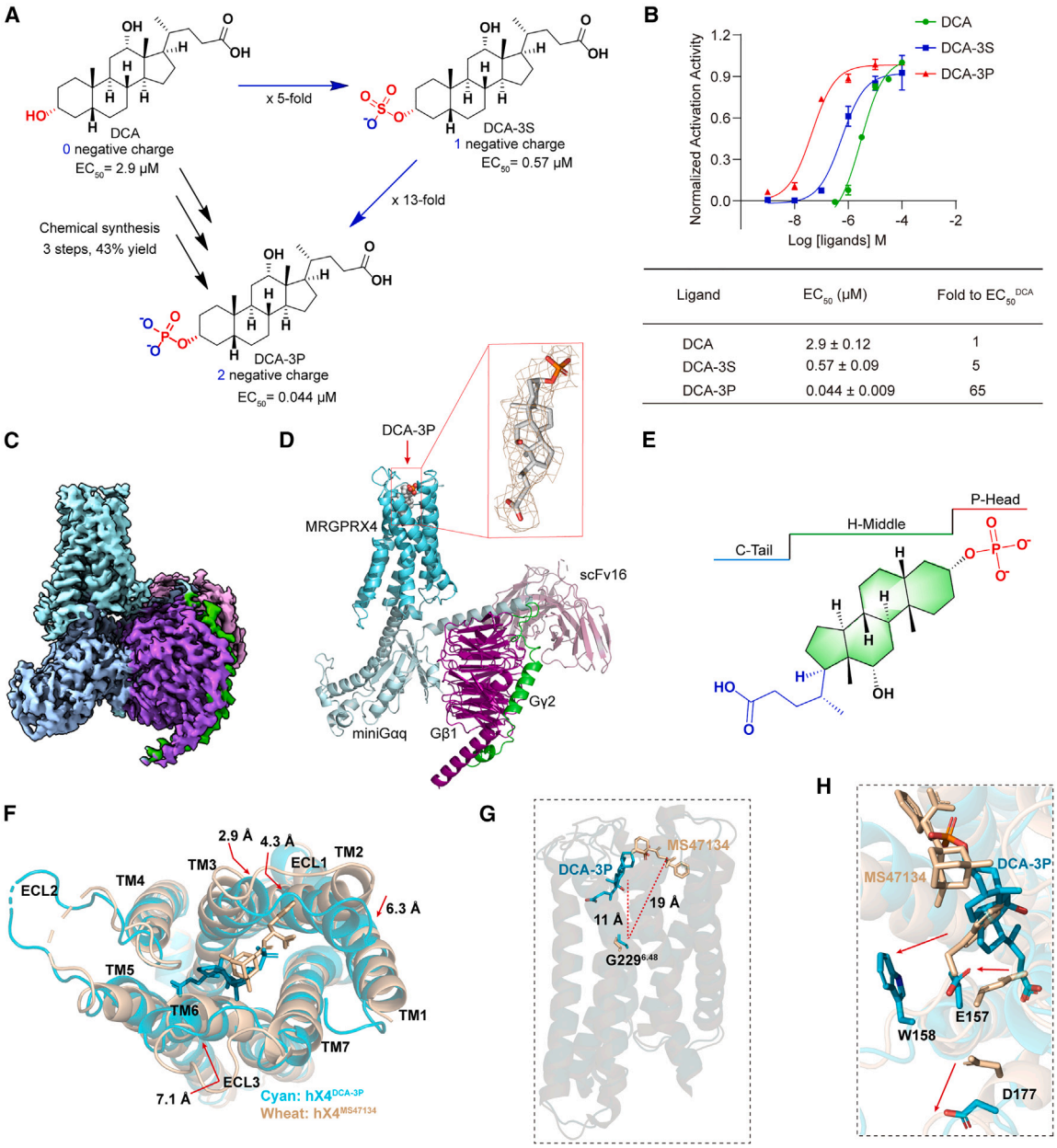

Figure 2. Rational design of DCA-3P, the overall structure of $X4^{DCA-3P}$, and DCA-3P binding pocket

(A) Overview of DCA optimization leading to the discovery of DCA-3P.

(B) DCA-3P exhibited increased potency as a hX4 agonist in the FLIPR-Ca^{2+} assay compared with DCA and DCA-3S. Data are represented as mean ± SEM, $n = 3$.

(C) Cryo-EM density map of $X4^{DCA-3P}$ complex with Gq.

(D) Overall structure of $X4^{DCA-3P}$ complex with G protein.

(E) DCA-3P's chemical structure. DCA-3P is divided into three parts: P-head (red), H-middle (green), and C-tail (blue).

(F) Structure comparison of $X4^{DCA-3P}$ (cyan) and $X4^{MS47134}$ (wheat). Displacements of the extracellular regions of $X4^{DCA-3P}$ relative to $X4^{MS47134}$ are highlighted with red arrows.

(G) The binding positions of DCA-3P and MS47134 are quite different in hX4.

(H) W158, E157, and D177 flip outward and produce ample space to accommodate the C-tail and H-middle of DCA-3P. The displacements of the three residues in hX4 are highlighted with red arrows.

See also Data S2.

Please cite this article in press as: Yang et al., Structure-guided discovery of bile acid derivatives for treating liver diseases without causing itch, Cell (2024), https://doi.org/10.1016/j.cell.2024.10.001

binding position in 5-HT_{2A}R,[72] A_{2A}R,[73] and β_2AR,[74] DCA-3P binds to hX4 at a position near the $G229^{6.48}$, which is relative to the canonical toggle switch $W336^{6.48}$ in 5-HT_{2A}R[72] (Data S2).

Additionally, unlike $W158^{ECL2}$, which was inserted inward in $X4^{MS47134}$, making $D177^{5.38}$ and $E157^{4.60}$ solvent-inaccessible and causing the insensitivity of hX4 to cationic agonists,[66] $W158^{ECL2}$, $D177^{5.38}$, and $E157^{4.60}$ in X4-DCA-3P rotated outward and freed up enough space to accommodate DCA-3P's H-middle and C-tail (Figure 2H).

BAs activate hX4 through several key amino acid residues

Similar to the previous studies,[66,67] the extracellular side of hX4 is rich in positive charges, and residues $R82^{2.60}$, $R86^{2.64}$, $R95^{3.25}$, and $K96^{3.26}$ forming a positively charged cleft accommodate the P-head of DCA-3P (Figures 3A and 3B). DCA-3P is anchored in the pocket via strong charge interactions with these residues (Figure 3B). Alanine mutations at these residues significantly decreased DCA-3P binding, supporting the essential functions of these residues in stabilizing the P-head (Figures 3C and S3A; Data S3). To explore how DCA-3S activates hX4, docking, and molecular dynamic (MD) simulations revealed that DCA-3S occupies the same binding pocket as DCA-3P, supported by similar potencies in mutagenesis studies (Figures S3A and S3B). While no significant difference in root-mean-square deviation (RMSD) was observed between hX4 bound to DCA-3P and DCA-3S, DCA-3S exhibited greater RMSD fluctuations, suggesting a weaker binding affinity (Figures 3D and S3C). This was confirmed by total MM/GBSA binding affinity calculations, with DCA-3P showing higher affinity than DCA-3S (Data S3).

Residues $R82^{2.60}$ and $R95^{3.25}$ are more critical than $R86^{2.64}$ in interacting with DCA-3P, as the distances between the DCA-3P's phosphorous atom and $R82^{2.60}$ or $R95^{3.25}$ remained stable in the MD experiments, while those involving $R86^{2.64}$ fluctuated (Figures S3D–S3F). Similarly, in DCA-3S, distances between sulfur and $R82^{2.60}$ or $R95^{3.25}$ are more stable than those with $R86^{2.64}$ (Figures S3D–S3F). Mutations R86A and R95A reduced DCA-3P's potency by 1,000-fold, whereas R86A reduced it by 100-fold (Figure S3G; Data S3), reinforcing the importance of $R82^{2.60}$, $R95^{3.25}$, and $R86^{2.64}$ in binding BA-type ligands (Figure S3H).

In the ligand-binding pocket, residues L246, I239, L235, Y254, V99, and F232 create a hydrophobic environment for non-polar interactions with the hydrophobic region (H-middle) of DCA-3P (Figure 3E). MD simulations showed that residues L235, F232, V99, and Y240 play key roles in binding DCA-3P (Data S3), and alanine mutations at these sites significantly reduced binding affinity (Figure 3F; Data S3).

Though no direct interactions were observed between hX4 and DCA-3P's C-tail in the cryo-EM structure, MD simulation revealed that R241 flips inward and forms strong salt bridge interactions with the carboxyl group of DCA-3P after 50 ns, further stabilizing the complex (Figures 3G, 3H, and S3H). Mutating R241 significantly decreased the DCA-3P's potency (Figure 3I; Data S3). The G protein structure in $X4^{DCA-3P}$ resembled that in $X4^{MS47134}$ (Data S2), and residues $V61^{2.39}$ and $Y130^{ICL2}$ of hX4 play an important role in binding Gαq by interacting with $Y243^{H5.23}$ of Gαq.[66] DCA-3P's binding induced similar conformations, emphasizing the importance of these residues for Gαq activation (Data S2).

OCA activates hX4 to induce itch

Pruritus is a common adverse effect of OCA,[22–26,28–31,33] limiting its clinical application. To understand the mechanism of OCA-induced itch, we explored whether OCA directly activates hX4 due to its structural similarity to CDCA and DCA (Figure 4A). In hX4-expressing HEK293T cells, OCA triggered a robust increase in intracellular Ca^{2+} levels, while no such response was observed in non-transfected cells (Figures S4A–S4C). Notably, the activation of hX4 by OCA displayed an EC_{50} value of 20–30 μM, like CDCA but considerably higher than glycine-conjugated CDCA (GCDCA), a prevalent CDCA conjugate in humans (Figure S4D). Intriguingly, unlike CDCA or GCDCA, OCA recruited and activated downstream β-arrestin signaling via hX4 (Figure S4D). Furthermore, OCA selectively activated hX4 without affecting other human MRGPRX receptors (Figure S4E). In hX4-expressing rat DRG neurons, OCA also induced a dose-dependent Ca^{2+} response, while non-transfected neurons remained unresponsive (Figures 4B–4F and S4F). Additionally, nearly half of the mS-positive neurons (mS^+) neurons from the humanized rats responded to OCA, while mS-negative neurons (mS^-) did not (Figures S4G–S4I). Collectively, we demonstrated that OCA selectively activates the itch receptor hX4, effectively mediating the activation of primary sensory neurons.

Subsequently, we tested whether OCA can induce itch by activating hX4. As expected, intradermal injection of OCA into the nape evoked significant scratching behavior in hX4 humanized rats while not provoking such behavior in littermate controls or WT rats (Figures 4G, 4H, S2A–S2D, S4J, and S4K). The scratching response evoked by OCA peaked within 15 min and declined slowly over time (Figure 4G). Furthermore, OCA evoked dose-dependent scratching behavior in humanized rats (Figure 4I). It did not induce a significant pain response when injected into the rat cheek (Figures S4L and S4M), suggesting OCA specifically causes itch in this animal model.

Intradermal injection of OCA evokes non-histaminergic itch in human subjects by activating hX4

To investigate whether OCA can directly induce itch in humans, we intradermally injected OCA into the forearms of human subjects. Remarkably, OCA induced a significant itch sensation, peaking within 10 min and gradually declining (Figures 4J–4L), mirroring the OCA-induced itch in the hX4 humanized rat (Figure 4G) and naturally occurring BAs in humans.[52] The itch intensity caused by OCA-induced followed a dose-dependent pattern (Figure 4M), consistent with the clinical trials.[11–14,16–21] Unlike histamine, OCA did not trigger a significant "red flare" (Figures 4N and 4O), and pretreatment with antihistamines did not reduce itch (Figures 4P and 4Q), suggesting OCA may directly activate itch nerve fibers and induce non-histaminergic itch in human subjects.

OCA-induced itch is not mediated by TGR5 or FXR

Previous studies have revealed that CDCA, the parent compound of OCA, robustly induces itch in humans.[52,75,76] Additionally, hX4 has been identified as a mediator of the itch-inducing

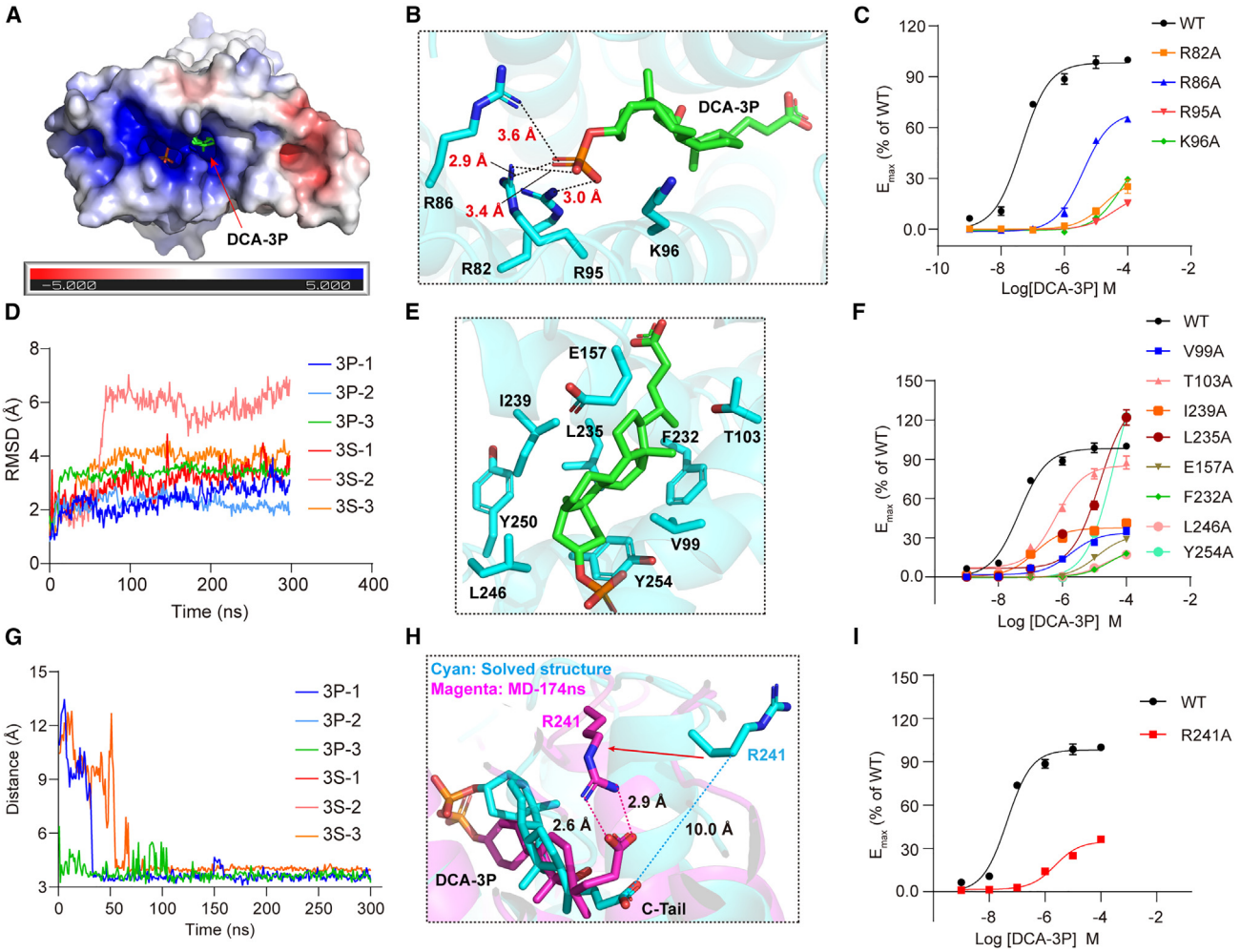

Figure 3. Molecular interactions of DCA-3P with hX4

(A) Electrostatic surface representation of the hX4 extracellular side calculated using the APBS plugin in PyMOL. Negative (-5 kTe^{-1}) and positive ($+5$ kTe^{-1}) are shown in red and blue, respectively.

(B) Interactions between the P-head of DCA-3P (green) and surrounding residues (cyan, sticks). The distances of those residues with phosphate groups are shown as black dashed lines.

(C) Alanine substituting hX4 residues interacting with P-head reduces the affinity.

(D) Root-mean-square deviation (RMSD) values of DCA-3P and DCA-3S during three 300 ns independent molecular dynamic (MD) simulations.

(E) Hydrophobic interactions of H-middle with hX4.

(F) Alanine substituting hX4 residues interacting with H-middle reduces the affinity.

(G) Distance between residue R241 and the carboxyl group of DCA-3P during MD simulations.

(H) R241 flips inward and forms interactions with the carboxyl of DCA-3P during MD simulations. The cryo-EM-solved structure and the structure at 174 ns in the simulations are shown as cyan and magenta, respectively.

(I) Validation of the function of R241.

Data are represented as means ± SEM, $n = 3$ for all panels.

See also Figure S3 and Data S2 and S3.

effects of naturally occurring BAs, including CDCA.[52] Our investigation found that CDCA and OCA activate hX4, TGR5, and FXR (Figures S5A and S5J). Interestingly, both the degree of hX4 activation and the resulting itch (Figures S5B and S5C) were comparable between OCA and CDCA, suggesting that OCA-evoked itch may be mediated by hX4.

To explore alternative mechanisms of OCA-induced itch, we examined related receptors (Figure 4A). Initially, we tested whether activating FXR alone could cause itch by applying tropifexor (TXR),[77] a highly potent non-steroidal FXR agonist currently in clinical trials for NASH and PBC[78] (NCT02516605). TXR exhibited an almost 70-fold greater potency than OCA in activating human FXR but did not activate TGR5 or hX4 (Figures S5D and S5K). Despite being administered at an equivalent concentration (a fold of the concentration used in the itch test to the EC_{50}; 5 μg in 25 μL, slightly exceeding the equivalent concentration of OCA)

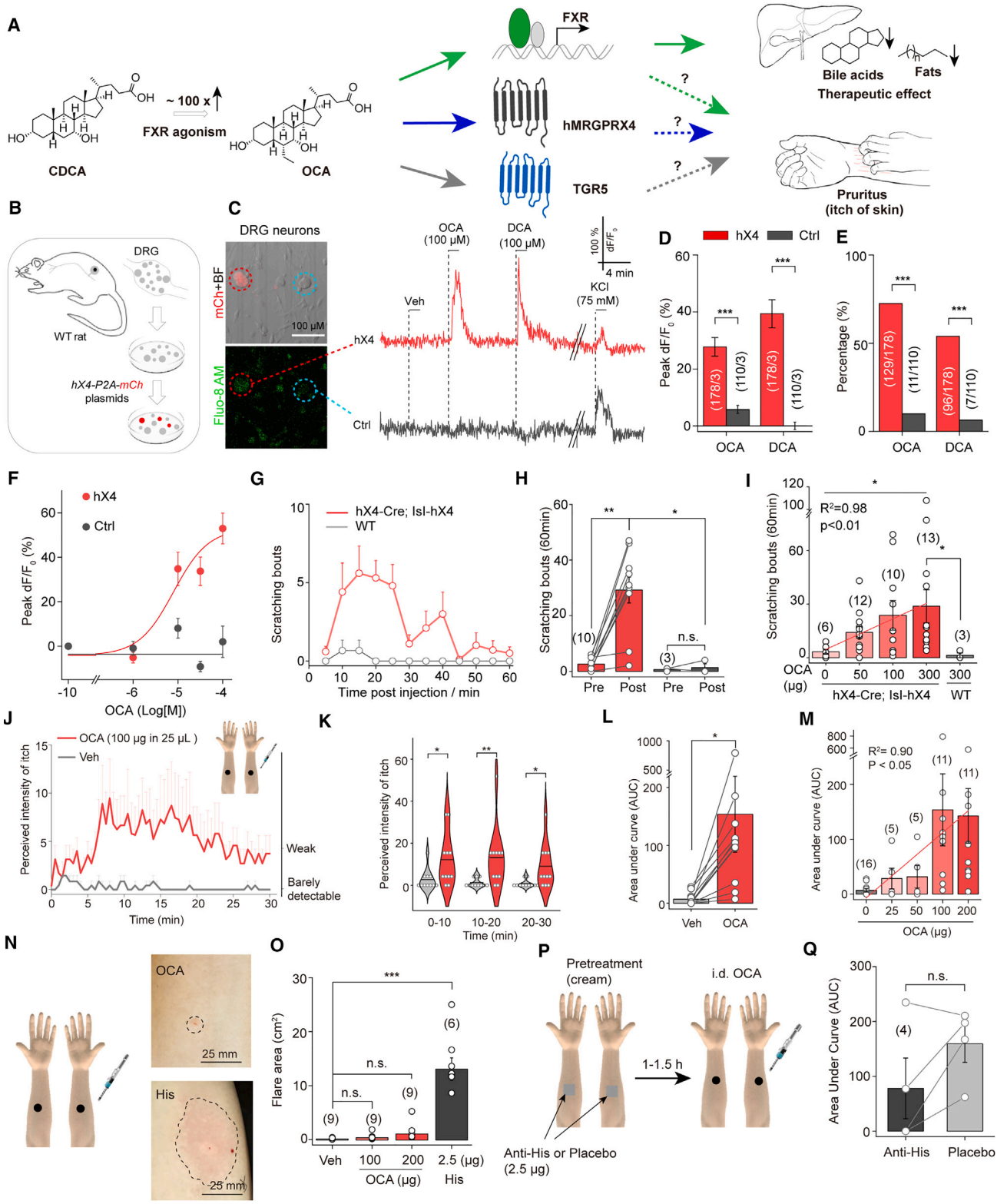

Figure 4. OCA directly evokes itch by activating hX4

(A) Putative mechanism by which OCA induces itch in humans. OCA activates FXR to reduce hepatic bile acids and fats. OCA-induced itch could be mediated by FXR, TGR5, and/or hX4.

(legend continued on next page)

higher than OCA's, TXR did not induce itch in human subjects (Figures S5E and S5F), strongly suggesting that activating FXR alone is not sufficient to trigger itch. Moreover, the rapid onset of OCA-induced itch (within 10–20 min) further supports this conclusion, as FXR typically mediates effects via regulating gene expression.[79]

Given OCA's potent activation of human TGR5, we also determined whether this receptor contributes to itch. INT-777, a TGR5-specific agonist[80] that does not activate FXR or hX4 (Figures S5G and S5L). Remarkably, intradermal injection of INT-777 failed to induce itch in humans (Figures S5H and S5I). This aligns with previous findings that TGR5 is expressed in satellite glial cells, not primary sensory neurons in human DRG.[52] In summary, OCA-induced itch in humans appears to be mediated by hX4 activation rather than FXR or TGR5.

OCA derivative C7, lacking the 3-OH group, maintains its capability to activate FXR but does not induce itch

With the potential mechanism underlying OCA-induced itch in mind, we hypothesized that mitigating its affinity for hX4 could ameliorate the pruritic side effect (Figure 5A). In the above, we resolved the structure of hX4 bounded with DCA-3P and elucidated the mechanism of BAs activating hX4. During the MD simulations, we found that the H-middle can rotate around the axis in some trajectories (Figures 5B and S5H), suggesting the binding of the BAs' H-middle is weak. Additionally, in the binding pose of BAs within hX4, carbon atoms 6 (CA6) and 7 (CA7) are oriented toward the solvent, allowing for modifications at these positions (Figure 5C). This explains why OCA, which features ethyl and hydroxyl groups at CA6 and CA7, respectively, can still activate hX4. Furthermore, docking studies revealed that OCA occupies the same position as DCA-3P in hX4 (Figure 5D).

Our structural analysis indicated that modifications to BAs' 3-OH are crucial for their affinity to hX4 (Figures 3B and 3C). We proposed that the 3-OH might also be vital for OCA activating hX4. Indeed, OCA activates hX4 with an EC_{50} of 26 ± 1.04 μM, and modifications of the 3-OH with sulfonate or phosphate groups significantly enhanced its affinity (Figures 5E and 5F). Thus, the 3-OH in OCA is also the essential group associated with its activity toward hX4. Previous studies have shown that 3-dCDCA (CDCA without 3-OH) can occupy the ligand-binding domain in FXR and has a comparable EC_{50} to CDCA,[81] indicating that the 3-OH may not be a prerequisite for activating FXR. Thus, modifying this group may be a precise strategy to maintain FXR activation while decreasing hX4 activation. Considering these results, we deleted the 3-OH from OCA to create C7 (Figure 5G). We then assessed C7's activity to FXR and hX4. As expected, C7 activates FXR with a potency like OCA while exhibiting no activation of hX4 (Figures 5H–5K; Table S1). Subsequent assessments confirmed that C7 effectively activates exogenous FXR in HEK293T cells (Figure 5J) and endogenous FXR in HepG2 cells (Figure 5K), albeit with slightly reduced potency compared with OCA.

To determine whether C7 mitigates the side effects associated with OCA, we evaluated its effect on hX4 activation at the cellular and animal levels. In cultured DRG neurons expressing hX4, C7 did not elicit an increase in intracellular Ca^{2+} levels, while OCA produced a robust response (Figures 5L–5N). Moreover, intradermal injection of C7 in hX4 humanized rats failed to induce scratching behavior (Figure 5O).

C7 activates FXR and regulates the expression of genes related to BA metabolism and lipid homeostasis

Previous studies have demonstrated that FXR agonism regulates the expression of genes involved in BA metabolism and lipid homeostasis,[82] underlying the clinical benefits of OCA in treating liver diseases such as PBC and NASH. To examine the genome-wide effects of activating FXR, we treated HepG2 cells with C7 and performed RNA sequencing (RNA-seq) analysis (Figure 6A). We found that C7 treatment significantly downregulated gene expression involved in the biosynthesis of BAs and fatty acids (FAs) (Figure 6B) while significantly upregulated gene expression related to bile secretion. Our analysis revealed that C7 and OCA altered the expression of 1,021 and 629 genes, respectively, compared with vehicle (Veh)-treated cells (Figure 6C). Notably, 376 genes exhibited overlapping between C7 and OCA treatments (Figures 6D and 6E). These changes were validated using quantitative real-time PCR (qPCR), confirming

(B–E) hX4 mediates OCA-induced activation of DRG neurons. The procedure of obtaining DRG neurons expressing hX4 (B). On the top-left, a brightfield (BF) image overlaid with the mCherry signal (red); on the bottom-left, a Fluo-8 AM signal, the neurons encircled by the dashed lines are hX4-positive (red) and hX4-negative (cyan). On the right, representative traces of the cells are indicated on the left (C). Peak dF/F_0 (D) and the percentage (E) of neurons that responded to OCA and DCA are defined as exceeding a 10% dF/F0 threshold. n = 110–178 neurons from 3 rats.

(F) Dose-dependent activation of hX4-expressing neurons stimulated by OCA.

(G–I) Intradermal (i.d.) injection of OCA into the neck of rats induced scratching behavior. Time course of scratching bouts after injected OCA in humanized and wild-type (WT) rats (G); total scratching bouts of humanized and WT rats within 60 min (H); and dose dependence of OCA inducing itching in humanized rats (I).

(J–L) Intradermal (i.d.) injection of OCA into the forearm evokes significant itch in human subjects. Time courses of perceived itch intensity evoked by OCA or Veh (J). Maximum itch intensity (peak) at the indicated times. Each dot represents an individual subject, and the black horizontal lines represent the mean values (K). The area under the curve (AUC) of the itch intensity traces (L).

(M) OCA evokes dose-dependent itch in human subjects (n = 5–16).

(N) Intradermal injections of OCA into the forearms of human subjects do not cause skin inflammation like histamine (His). The encircled area in the enlarged images indicates the flare area.

(O) Quantification of flare area was measured in subjects after an intradermal injection of Veh, OCA, or His. n = 6–9 per group.

(P) An antihistamine (Anti-His) cream or placebo (cold cream) was applied, followed by an intradermal injection of OCA (200 μg).

(Q) Topical antihistamine cream does not significantly reduce OCA-induced itch in human subjects. n = 4.

For all panels, data are presented as the mean ± SEM. $^*p < 0.05$, $^{**}p < 0.01$, $^{***}p < 0.001$, and n.s., not significant ($p > 0.05$); unpaired two-way Student's t test (D), two-proportion z-test (E), Wilcoxon matched-pairs signed-rank test, and Mann-Whitney test (H and K), Kruskal-Wallis ANOVA test (I), one-way ANOVA test (O), or paired two-way Student's t test (L and Q).

See also Figures S2, S4, and S5.

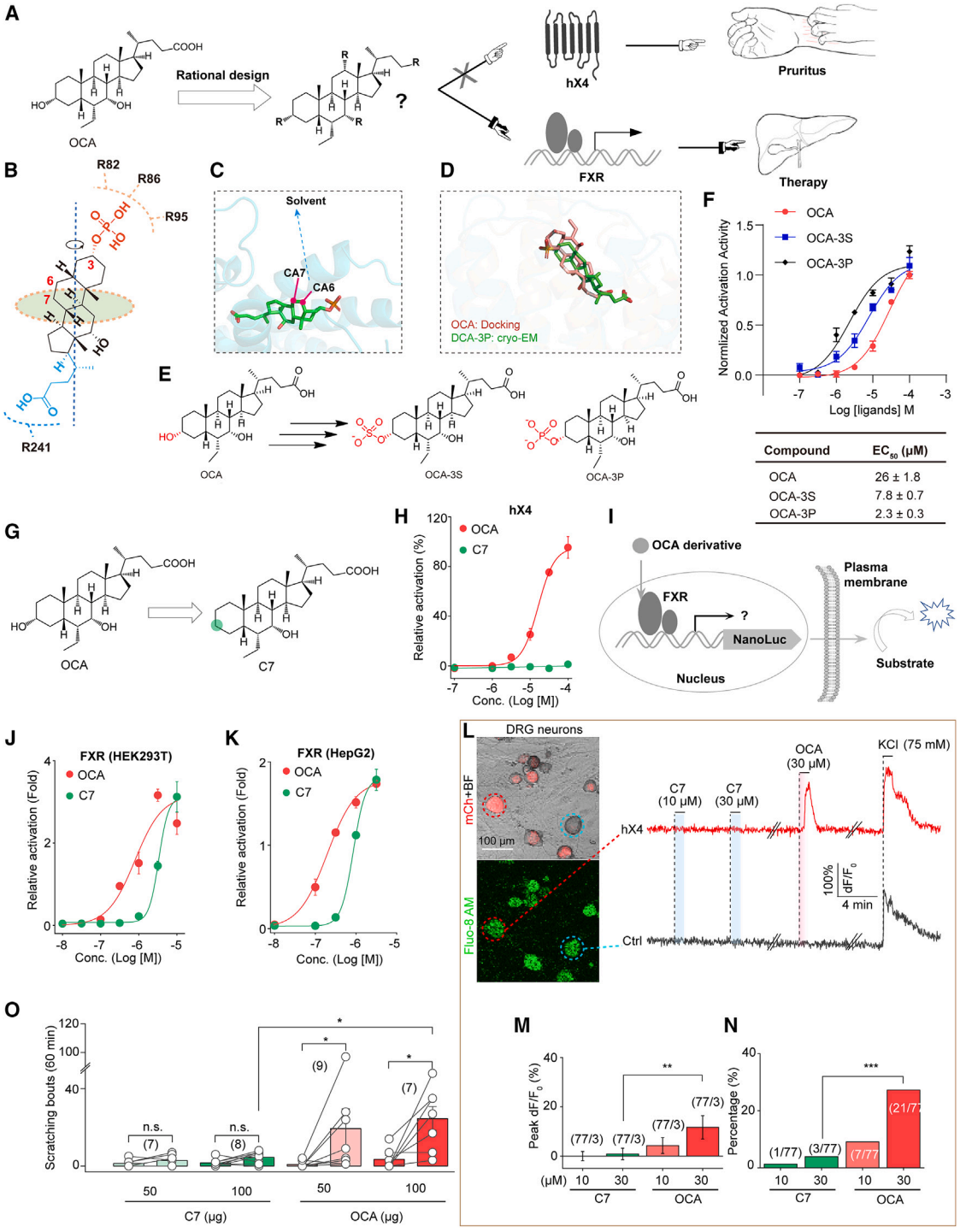

Figure 5. Rational design of OCA derivatives that reduce itch but still activate FXR

(A) OCA is an FXR agonist derived from CDCA with modifications at C6 and C7. We aimed to decrease OCA's affinity for hX4 but retain its activity for FXR.

(B) The P-head and C-tail of DCA-3P were anchored by R82-R86-R95 and R241, respectively. The H-middle can rotate around the axis during MDs.

(C) CA6 and CA7 of DCA-3P toward the solvent in the hX4 pocket.

(D) OCA (red) was docked into the binding pocket of hX4 and occupied the same position as DCA-3P (green).

(E) Derivate OCA to generate OCA-3S and OCA-3P.

(F) OCA-3S and OCA-3P increased the affinity to hX4.

(legend continued on next page)

that C7 significantly downregulated *Cyp7a1* and upregulated *Nr0b2* and *Abcb11* (Figure 6F), consistent with our RNA-seq data.

We also examined the effects of C7 on gene expression and hepatic toxicity *in vivo* (Figure S6A). Oral administration of C7 (5 to 30 mg/kg) dose-dependently increased the expression of hepatic *Nr0b2* and *Abcb11* (Figure S6B). Even at the highest dose, C7 did not elevate serum transaminases (Figures S6C and S6D), including alkaline phosphatase (ALP), alanine transaminase (ALT), and aspartate transaminase (AST), suggesting no detectable hepatic toxicity.

C7 alleviates liver injury and fibrosis in cholestasis models

To examine whether C7 can reduce liver injury in rat models of cholestasis induced by α-naphthylisothiocyanate (ANIT), which damages biliary epithelial cells and impairs BAs transporter function,[83] we conducted transcriptomic analysis, biomarker measurements, and liver pathology utilizing rat models treated with C7 (Figure 7A). C7 and OCA downregulated gene expression is associated with BA biosynthesis and acute inflammatory response, but distinct gene expression patterns indicate reduced BA levels and alleviated inflammation (Figures 7B, S6E, and S6F). These structural distinctions may explain the varied gene expression profiles upon FXR activation, likely due to structure-dependent interactions with coactivators.[84–86] Notably, compared with OCA, C7 caused more significant changes in the expression of genes involved in bile secretion, such as *Nr0b2*, *Abcb11*, and *Abcb4* (Figure 7C). qPCR analysis further confirmed that C7 effectively reduced the expression of genes related to BAs synthesis (*Cyp7a1* and *Cyp8b1*) and proinflammation (*Cxcl1* and *Cxcl2*), while enhancing BA transporters expression (Figure 7C).

Clinical studies have indicated that OCA reduces serum transaminases in patients with PBC.[22–24] Herein, both C7 and OCA significantly reversed the ANIT-induced elevation in serum biomarkers of liver injury, including total bilirubin (TB), ALT, and AST levels, demonstrating hepatoprotection effects (Figure 7D). Histological evaluation revealed that C7 significantly attenuated the liver damage, including hepatic parenchymal necrosis and inflammatory cell infiltration caused by ANIT (Figures 7E and 7F). Interestingly, 10 mg/kg OCA did not significantly mitigate serum TB or ALT levels or alleviate liver injury as C7 (Figures 7D and 7F).

In contrast to toxin-induced acute liver injury, bile duct ligation (BDL) is a well-established model for studying extrahepatic cholestasis and the consequences of liver fibrosis.[84] C7 was also evaluated in the mouse BDL model (Figure S6G). Although serum ALT levels in BDL mice remained unchanged with C7 (3 or 10 mg/kg) and OCA (3 mg/kg) treatment, both compounds significantly prevented the increase in TB levels (Figure S6H). Moreover, both C7 (10 mg/kg) and OCA (3 mg/kg) substantially reduced cirrhosis with portal fibrosis from acute obstructive jaundice,[84] as measured by Sirius red staining (Figures S6I and S6J). Notably, 3 mg/kg OCA significantly reduced liver fibrosis in BDL mice, potentially due to a difference in FXR affinity.

In summary, these *in vivo* results strongly underscore the therapeutic potential of C7 in providing clinically significant protection against cholestasis, evidenced by improved serum markers and liver histology. C7 appears to have even more substantial benefits than OCA in some aspects, possibly attributable to extended drug exposure and increased bioavailability (Data S4). Like OCA, C7 can be transported by human BA transporters such as ASBT, NTCP, and OSTα/β, demonstrating its capacity for enterohepatic cycling (Data S4).

C7 alleviates hepatic steatosis and fibrosis in NASH models

Given C7's anti-inflammatory properties, it shows potential as a treatment for NASH. To evaluate its effectiveness in alleviating chronic steatosis and fibrosis, key NASH symptoms, we used rat models induced by thioacetamide (TAA)[85] (Figure 7G). Compared with the untreated group (Ctrl), TAA administration (Veh) significantly upregulated the expression of genes related to collagen production, fibrosis progression (*Timp3*, *Col3a1*, *Acta2*, and *Tgfb1*), and lipogenesis (*Acaca*, *Gpat3*, and *Lpin*) (Figure 7H), and both C7 and OCA significantly downregulated these genes expression (Figures 7H, S7A, and S7B). qPCR analysis of liver tissue further confirmed that both treatments reduced gene expression linked to lipogenesis and fibrosis (Figure 7I).

TAA-induced elevations in serum TB, ALT, and AST levels were significantly mitigated in rats receiving C7 treatment (Figure 7J). While FXR is known to regulate TG levels,[13,86] our experiments did not show an increase in serum TG levels following TAA exposure as reported.[87] OCA, but not C7, significantly reduced serum TG levels (Figure 7J). Interestingly, C7 considerably elevated total serum cholesterol (TC), high-density lipoprotein cholesterol (HDL-C), and LDL-C levels compared with the Veh group (Figure 7J), a phenomenon observed with other FXR agonists in clinical trials.[26,27,78,88,89] Histological analysis showed that C7 significantly reduced TAA-induced liver injury (Figures S7C and S7D), fibrosis (Figures 7K and 7L), and hepatic steatosis (Figures 7K and 7L). These findings suggest that C7 could alleviate NASH symptoms.

(G) C7 was derived from OCA by deleting the hydroxyl group at C3.
(H) Dose-response curves of hX4 activation in response to OCA and C7.
(I–K) Dose-response curves of FXR activation (J) and endogenous FXR activation in HepG2 cells (K) by OCA and C7.
(L–N) Representative traces of Fluo-8 AM fluorescence recording in cultured rat DRG neurons expressing hX4 (hX4-positive, red) or not (hX4-negative, cyan) (L). Summary of peak dF/F_0 (M) and the percentage (N) of neurons that responded to C7 and OCA. Neurons having a response of $dF/F_0 > 10\%$ are defined as responsive. $n = 77$ neurons from 3 coverslips.
(O) C7 does not induce scratching behavior in humanized rats. $n = 7–9$ per group.
For all panels, data are presented as the mean ± SEM; $^*p < 0.05$, $^{**}p < 0.01$, $^{***}p < 0.001$, and n.s., not significant ($p > 0.05$); paired two-way Student's t test (M), two-proportion z-test (N), Wilcoxon matched-pairs signed-rank tests, and Mann-Whitney test (O).
See also Table S1.

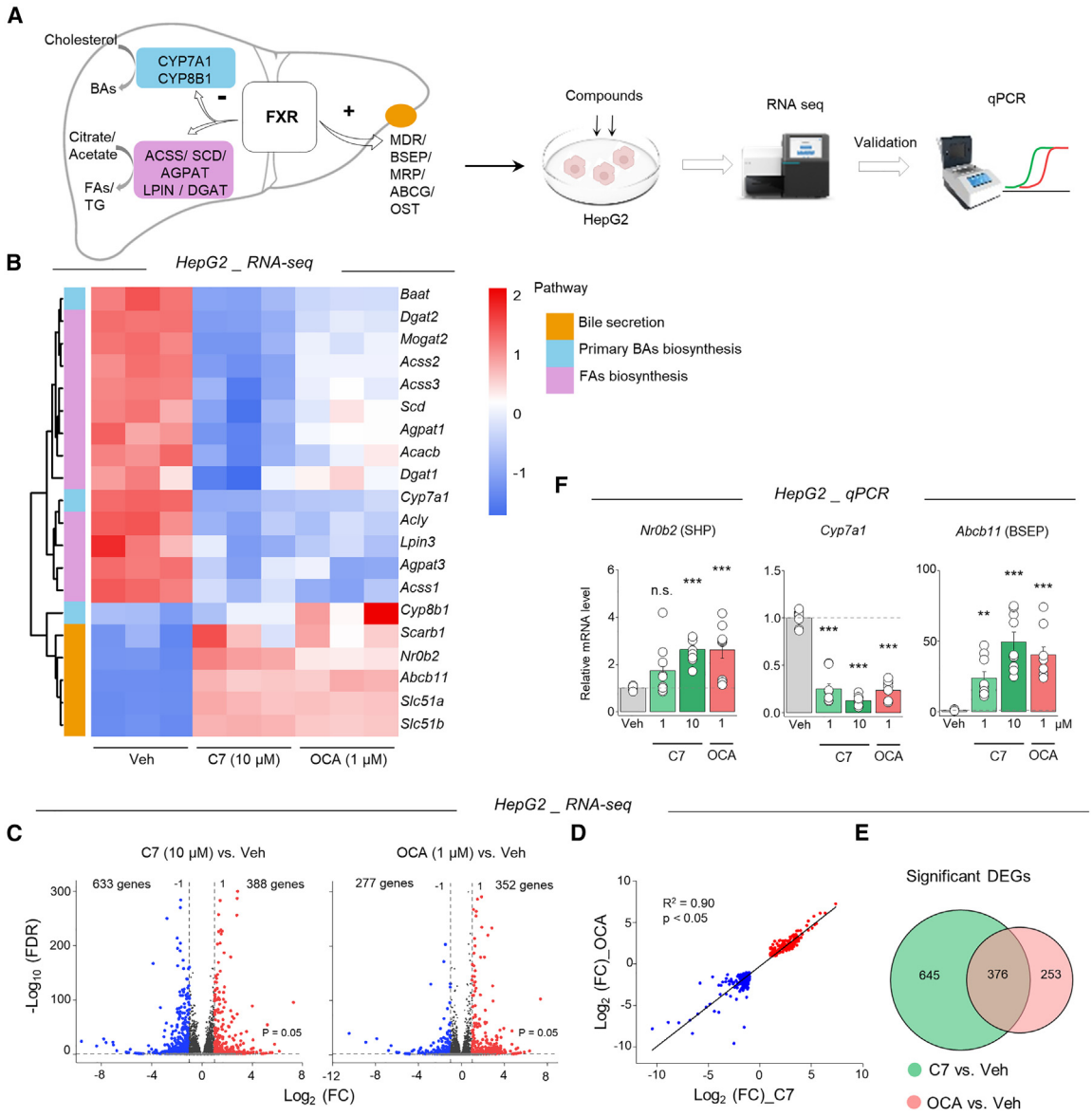

Figure 6. C7 regulates the expression of genes downstream of FXR

(A) Schematic diagram depicting how FXR regulates hepatic BAs and fatty acid (FA) metabolism. "−," inhibit; "+," Activate.

(B) Heatmap and clustering analysis of representative differentially expressed genes (DEGs) in HepG2 cells following treatment with 10 μM C7 or 1 μM OCA. $n = 3$ per group.

(C) Volcano plots showing the distribution of all DEGs measured in HepG2 treated with C7 or OCA. Red, upregulated; blue, downregulated. The vertical dashed lines at −1 and 1 indicate a 2-fold change (FC) threshold in gene expression. The horizontal dashed line indicates a false discovery rate (FDR, adjusted p value) of 0.05. The number of significantly upregulated and downregulated genes is shown.

(D) Correlation between DEGs in HepG2 treated with OCA versus C7.

(E) Venn diagram summarizing the number of DEGs in response to C7 (green) or OCA (red).

(F) qPCR analysis of the indicated DEGs involved in BA metabolism relative to the Veh group. $n = 5–10$ per group.

For all panels, $^{*}p < 0.05$, $^{**}p < 0.01$, $^{***}p < 0.001$, and n.s., not significant ($p > 0.05$) versus the corresponding Veh group (one-way ANOVA).

See also Figure S6 and Data S4.

NASH pathogenesis is explained by the "multiple-parallel hit" model, wherein lipid accumulation renders hepatocytes more susceptible to secondary injuries, such as oxidative stress or a self-immune response.[90,91] To create a more clinically relevant NASH model, we subjected mice to a high-fat diet (HFD) for 10 weeks to induce obesity, followed by carbon tetrachloride injections for four weeks[92] (Figure S7E). Consistently, C7 (30 mg/kg) significantly reduced serum ALT and AST levels in NASH mice (Figure S7F), as well as obesity-associated increases in serum TG and TC (Figure S7F). Given metabolic

Please cite this article in press as: Yang et al., Structure-guided discovery of bile acid derivatives for treating liver diseases without causing itch, Cell (2024), https://doi.org/10.1016/j.cell.2024.10.001

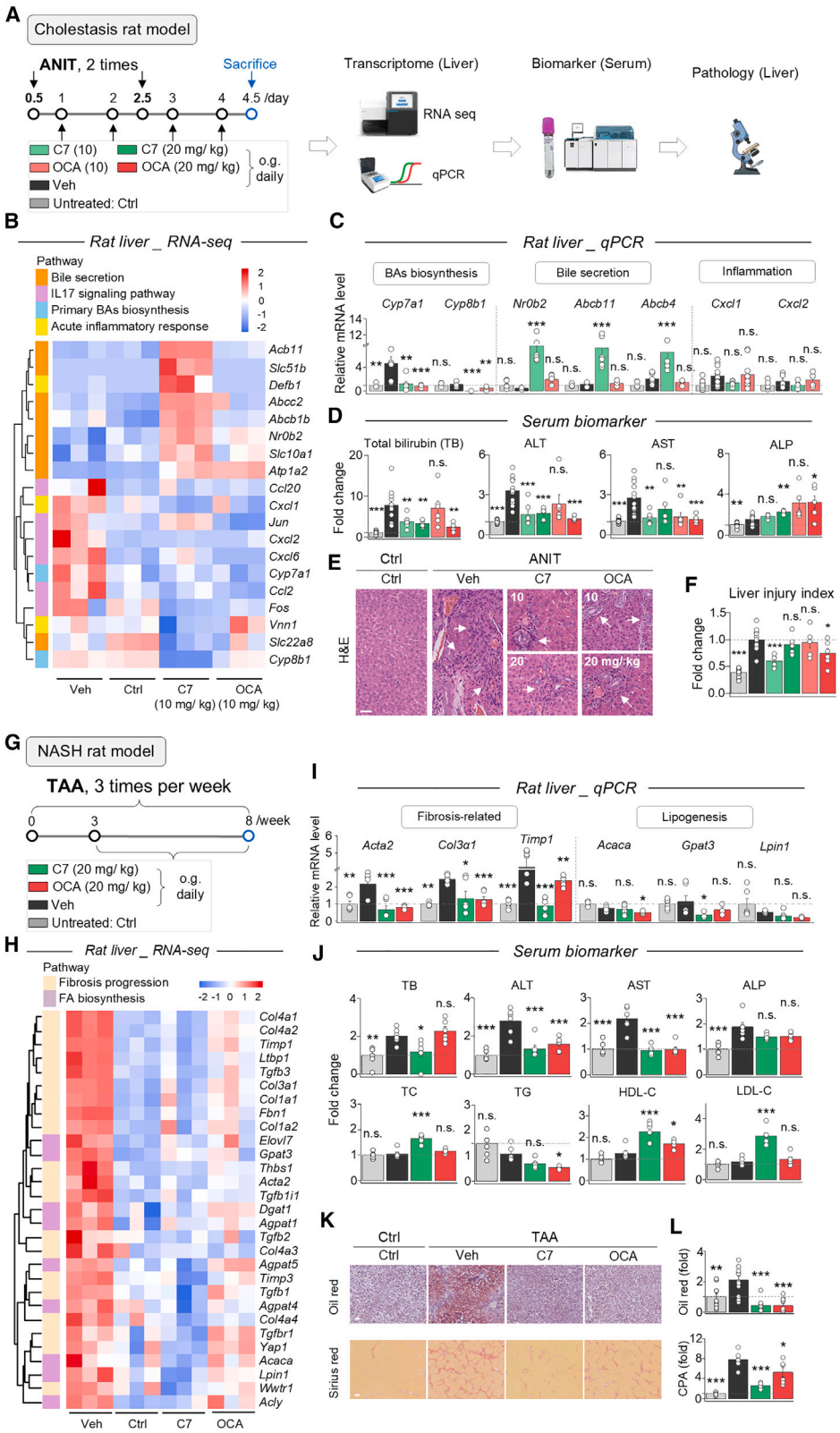

(legend on next page)

crosstalk between the liver and adipose tissue plays a role in the pathogenesis of NASH,[93,94] NASH mice exhibited significantly increased ratios of gonadal white adipose tissue (gWAT) and inguinal white adipose tissue (iWAT) to body weight (Figure S7G). Histologically, both C7 and OCA effectively reduced liver fibrosis, though only high-dose OCA reduced the NAFLD activity score (NAS) (Figures S7H–S7J). In summary, these results suggest that C7 is a promising candidate for NASH treatment without the undesirable side effect of itch.

DISCUSSION

CP is a prevalent symptom in liver disease patients, significantly impacting their quality of life. While previous studies have linked BAs and hX4 to CP, the underlying mechanisms remain poorly understood. Here, we identified the 3-sulfated BAs as endogenous ligands of hX4, essential in aggravating pruritus. We also developed DCA-3P, a synthetic analog with a higher affinity for hX4 than DCA and DCA-3S, owing to its P-head, which carries more negative charges. The cryo-EM structure of the hX4 complexed with DCA-3P highlighted crucial interactions, particularly the significance of the 3-OH in BAs for activating hX4. This discovery marks the new ligand-binding into the canonical pocket of MRGPR family receptors.

NASH is a globally prevalent disease with limited treatment options. Although OCA, an FXR agonist, is the most advanced treatment, its clinical use is limited by the severe itch side effect. Our findings showed that hX4, not FXR or TGR5, mediates OCA-induced itch in humans. Based on the structural basis of BAs activating hX4, we designed C7, an OCA derivative with comparable FXR affinity but without hX4 activation, which prevented itch.

Previously, Sepe et al. and Xiao et al. explored BA derivatives for NASH but did not eliminate the itch side effect.[95,96] While several non-steroidal FXR agonists are currently being evaluated for clinical evaluation, such as TXR,[78] EDP-305,[97] Cilofecor,[88] MET409,[89] and Vonafexor (NCT03812029). OCA remains most extensively studied regarding its confirmed safety, tolerability, and pharmacokinetics through numerous clinical trials, with approval from the FDA for PBC treatment. Therefore, we propose that C7 holds potential as a treatment option for liver diseases, with further clinical trials warranted to explore its efficacy and safety profile.

In summary, this study revealed BAs' role in CP, the structural basis of how BAs activate hX4, identified hX4 as the primary receptor for OCA-induced itch, and developed C7 as a promising candidate for treating NASH without pruritus.

Limitations of the study

This work uncovered that 3-sulfated BAs enhance their affinity to hX4, aggravating cholestatic itch. For BAs to induce itch, they must accumulate in the skin; however, itch fibers are primarily located in the epidermis and do not directly contact the circulation. In this study, we conducted scratching behavioral experiments using higher BA concentrations than those found in plasma, demonstrating that 3-sulfated BAs can aggravate itch despite the unknown levels of BAs in the skin. Therefore, the physiological relevance between plasma BA levels, their accumulation in the skin, and itch remains to be investigated. Additionally, based on the structural insights, we developed C7, which retains the activity toward FXR to treat liver disease but lacks the activity toward hX4 activation, preventing itch side effects. However, C7 still requires further optimization for clinical application.

RESOURCE AVAILABILITY

Lead contact

Further information and requests for resources should be directed to and will be fulfilled by the lead contact, Xiaoguang Lei (xglei@pku.edu.cn).

Materials availability

Further information and requests for any reagents generated in this study, including compounds, plasmids, and cell lines, are available upon reasonable request from the lead contact.

Data and code availability

- The cryo-EM overall and local refinement maps for MRGPRX4^{DCA-3P} have been deposited in the electron microscopy data bank with accession codes EMD-36890 and EMD-37191, respectively.
- The atomic coordinates for MRGPRX4^{DCA-3P}-Gq and MRGPRX4^{DCA-3P} have been deposited in the protein data bank under accession codes 8K4S and 8KEX, respectively.

ACKNOWLEDGMENTS

We thank X. Huang, B. Zhu, X. Li, and L. Chen at the Center for Biological Imaging, Core Facilities for Protein Science, at the Institute of Biophysics,

Figure 7. C7 reduces liver injury, steatosis, and fibrosis in several animal models

(A–F) Treatment of C7 in rats with ANIT-induced cholestasis. Scheme of the experimental design (A). Heatmap and clustering analysis of representative DEGs in ANIT-treated rats treated with 10 mg/kg C7, OCA, or Veh. $n = 3$ per group (B). qPCR analysis of genes related to inflammation and BA metabolism in the indicated groups relative to Ctrl. $n = 4$–12 per group (C). Fold change in serum total bilirubin (TB), ALT, AST, and ALP concentrations compared with Ctrl. $n = 6$–12 per group (D). H&E-stained liver sections were obtained from rats in the indicated groups. Arrows indicate hepatocyte damage and immune cell infiltration: scale bar, 50 μm (E). Quantifying the liver injury patterns in the indicated groups, expressed relative to the Veh group. $n = 5$–12 per group (F).

(G–L) Treatment of C7 in rats with TAA-induced model of liver fibrosis and steatosis. Scheme of the experimental design (G). Heatmap and clustering analysis of representative DEGs in TAA-treated rats treated with 20 mg/kg C7, OCA, or Veh. $n = 3$ per group (H). qPCR analysis of the indicated genes related to fibrosis progression and lipid metabolism measured in the indicated group relative to the Ctrl group. $n = 6$ per group (I). Fold change in serum TB, ALT, AST, ALP, total cholesterol (TC), TG, high-density lipoprotein cholesterol (HDL-C), and low-density lipoprotein cholesterol (LDL-C) concentrations relative to the Ctrl. $n = 6$ per group (J). Oil red-stained (top row) and Sirius red-stained (bottom row) liver sections were obtained from the indicated groups: scale bars, 50 μm (K). Quantification of oil red-positive area (top) and Sirius red-positive area (collagen proportionate area, CPA) in the indicated groups, expressed relative to the Veh group. $n = 6$ per group (L).

For all panels, $^{*}p < 0.05$, $^{**}p < 0.01$, $^{***}p < 0.001$, and n.s. = not significant ($p > 0.05$) versus the corresponding Veh group (one-way ANOVA).

See also Figures S4, S6, and S7.

Chinese Academy of Sciences, for support in cryo-EM data collection. We thank Y. Rao (Peking University) for supporting the FLIPR device. This work is funded by grants from the National Key Research and Development Program of China (2022YFC3401500 and 2022YFC2502500 to X.L., 2022YFE0108700 to Y.L., and 2022YFC2304402 to Y.C. and H.Z.), the National Natural Science Foundation of China (22337002, 92253305, and 22193073 to X.L.; 31925017 to Y.L.; and 22177006 to J.F.), the Beijing National Laboratory for Molecular Sciences (BNLMS-CXX-202106 to X.L.), the Chinese Institutes for Medical Research, Beijing (CX23YZ18 to X.L.), the Beijing Municipal Science & Technology Commission (Z220009 to Y.L.), the State Key Laboratory of Membrane Biology at Peking University School of Life Sciences, the New Cornerstone Science Foundation through the New Cornerstone Investigator Program and the XPLORER PRIZE (to X.L. and Y.L.), and the Beijing Natural Science Foundation (7232081 to Y.C. and H.Z.).

AUTHOR CONTRIBUTIONS

X.L. conceived the original concept and initiated the project; X.L. and Y.L. managed the whole project; J.Y., T.Z., Y.L., and X.L. designed and performed most of the experiments; H.Z. and Y.C. collected the patients' plasma samples; J.Y. analyzed the patients' samples with the help from Y.B.; J.F., J.Y., and Z.Y. solved the cryo-EM structure; H.K. conducted the computational analysis; T.Z., J.Y. and G.L. conducted the FLIPR-Ca^{2+} assay under the guidance of Y.L.; T.Z., G.L., F.G., and Y.L. performed the animal experiments; Y.S., Xin Wang, and S.L. synthesized the compounds used in this project with the help from Xiaoming Wang.; J.Y., T.Z., Y.L., and X.L. wrote the manuscript with inputs from all authors.

DECLARATION OF INTERESTS

The authors declare no competing interests.

STAR★METHODS

Detailed methods are provided in the online version of this paper and include the following:

SUPPLEMENTAL INFORMATION

Supplemental information can be found online at https://doi.org/10.1016/j.cell.2024.10.001.

Received: February 18, 2024
Revised: June 11, 2024
Accepted: October 2, 2024
Published: October 29, 2024

REFERENCES

1. Younossi, Z.M., Golabi, P., de Avila, L., Paik, J.M., Srishord, M., Fukui, N., Qiu, Y., Burns, L., Afendy, A., and Nader, F. (2019). The global epidemiology of NAFLD and NASH in patients with type 2 diabetes: A systematic review and meta-analysis. J. Hepatol. *71*, 793–801. https://doi.org/10.1016/j.jhep.2019.06.021.
2. Lazarus, J.V., Mark, H.E., Anstee, Q.M., Arab, J.P., Batterham, R.L., Castera, L., Cortez-Pinto, H., Crespo, J., Cusi, K., Dirac, M.A., et al. (2022). Advancing the global public health agenda for NAFLD: a consensus statement. Nat. Rev. Gastroenterol. Hepatol. *19*, 60–78. https://doi.org/10.1038/s41575-021-00523-4.
3. Dufour, J.-F., Scherer, R., Balp, M.-M., McKenna, S.J., Janssens, N., Lopez, P., and Pedrosa, M. (2021). The global epidemiology of nonalcoholic steatohepatitis (NASH) and associated risk factors–A targeted literature review. Endocr. Metab. Sci. *3*, 100089. https://doi.org/10.1016/j.endmts.2021.100089.
4. Younossi, Z.M., Stepanova, M., Ong, J., Trimble, G., AlQahtani, S., Younossi, I., Ahmed, A., Racila, A., and Henry, L. (2021). Nonalcoholic Steatohepatitis Is the Most Rapidly Increasing Indication for Liver Transplantation in the United States. Clin. Gastroenterol. Hepatol. *19*, 580–589.e5. https://doi.org/10.1016/j.cgh.2020.05.064.
5. Garber, K. (2019). The new liver epidemic. Nat. Biotechnol. *37*, 209–214. https://doi.org/10.1038/s41587-019-0047-9.
6. Makishima, M., Okamoto, A.Y., Repa, J.J., Tu, H., Learned, R.M., Luk, A., Hull, M.V., Lustig, K.D., Mangelsdorf, D.J., and Shan, B. (1999). Identification of a nuclear receptor for bile acids. Science *284*, 1362–1365. https://doi.org/10.1126/science.284.5418.1362.
7. Parks, D.J., Blanchard, S.G., Bledsoe, R.K., Chandra, G., Consler, T.G., Kliewer, S.A., Stimmel, J.B., Willson, T.M., Zavacki, A.M., Moore, D.D., and Lehmann, J.M. (1999). Bile acids: natural ligands for an orphan nuclear receptor. Science *284*, 1365–1368. https://doi.org/10.1126/science.284.5418.1365.
8. Wang, H., Chen, J., Hollister, K., Sowers, L.C., and Forman, B.M. (1999). Endogenous bile acids are ligands for the nuclear receptor FXR/BAR. Mol. Cell *3*, 543–553. https://doi.org/10.1016/s1097-2765(00)80348-2.
9. Myant, N.B., and Mitropoulos, K.A. (1977). Cholesterol 7 alpha-hydroxylase. J. Lipid Res. *18*, 135–153. https://doi.org/10.1016/S0022-2275(20)41693-1.
10. Goodwin, B., Jones, S.A., Price, R.R., Watson, M.A., McKee, D.D., Moore, L.B., Galardi, C., Wilson, J.G., Lewis, M.C., Roth, M.E., et al. (2000). A regulatory cascade of the nuclear receptors FXR, SHP-1, and LRH-1 represses bile acid biosynthesis. Mol. Cell *6*, 517–526. https://doi.org/10.1016/s1097-2765(00)00051-4.
11. Inagaki, T., Choi, M., Moschetta, A., Peng, L., Cummins, C.L., McDonald, J.G., Luo, G., Jones, S.A., Goodwin, B., Richardson, J.A., et al. (2005). Fibroblast growth factor 15 functions as an enterohepatic signal to regulate bile acid homeostasis. Cell Metab. *2*, 217–225. https://doi.org/10.1016/j.cmet.2005.09.001.

12. Ananthanarayanan, M., Balasubramanian, N., Makishima, M., Mangelsdorf, D.J., and Suchy, F.J. (2001). Human bile salt export pump promoter is transactivated by the farnesoid X receptor/bile acid receptor. J. Biol. Chem. *276*, 28857–28865. https://doi.org/10.1074/jbc.M011610200.

13. Clifford, B.L., Sedgeman, L.R., Williams, K.J., Morand, P., Cheng, A., Jarrett, K.E., Chan, A.P., Brearley-Sholto, M.C., Wahlström, A., Ashby, J.W., et al. (2021). FXR activation protects against NAFLD via bile-acid-dependent reductions in lipid absorption. Cell Metab. *33*, 1671–1684.e4. https://doi.org/10.1016/j.cmet.2021.06.012.

14. Ma, K., Saha, P.K., Chan, L., and Moore, D.D. (2006). Farnesoid X receptor is essential for normal glucose homeostasis. J. Clin. Invest. *116*, 1102–1109. https://doi.org/10.1172/JCI25604.

15. Cariou, B., van Harmelen, K., Duran-Sandoval, D., van Dijk, T.H., Grefhorst, A., Abdelkarim, M., Caron, S., Torpier, G., Fruchart, J.C., Gonzalez, F.J., et al. (2006). The farnesoid X receptor modulates adiposity and peripheral insulin sensitivity in mice. J. Biol. Chem. *281*, 11039–11049. https://doi.org/10.1074/jbc.M510258200.

16. Lee, J.M., Wagner, M., Xiao, R., Kim, K.H., Feng, D., Lazar, M.A., and Moore, D.D. (2014). Nutrient-sensing nuclear receptors coordinate autophagy. Nature *516*, 112–115. https://doi.org/10.1038/nature13961.

17. Seok, S., Fu, T., Choi, S.E., Li, Y., Zhu, R., Kumar, S., Sun, X., Yoon, G., Kang, Y., Zhong, W., et al. (2014). Transcriptional regulation of autophagy by an FXR-CREB axis. Nature *516*, 108–111. https://doi.org/10.1038/nature13949.

18. Fiorucci, S., Biagioli, M., Zampella, A., and Distrutti, E. (2018). Bile Acids Activated Receptors Regulate Innate Immunity. Front. Immunol. *9*, 1853. https://doi.org/10.3389/fimmu.2018.01853.

19. Wang, Y.D., Chen, W.D., Wang, M., Yu, D., Forman, B.M., and Huang, W. (2008). Farnesoid X receptor antagonizes nuclear factor kappaB in hepatic inflammatory response. Hepatology *48*, 1632–1643. https://doi.org/10.1002/hep.22519.

20. Fiorucci, S., Biagioli, M., Baldoni, M., Ricci, P., Sepe, V., Zampella, A., and Distrutti, E. (2021). The identification of farnesoid X receptor modulators as treatment options for nonalcoholic fatty liver disease. Expert Opin. Drug Discov. *16*, 1193–1208. https://doi.org/10.1080/17460441.2021.1916465.

21. Pellicciari, R., Fiorucci, S., Camaioni, E., Clerici, C., Costantino, G., Maloney, P.R., Morelli, A., Parks, D.J., and Willson, T.M. (2002). 6alpha-ethyl-chenodeoxycholic acid (6-ECDCA), a potent and selective FXR agonist endowed with anticholestatic activity. J. Med. Chem. *45*, 3569–3572. https://doi.org/10.1021/jm025529g.

22. Hirschfield, G.M., Mason, A., Luketic, V., Lindor, K., Gordon, S.C., Mayo, M., Kowdley, K.V., Vincent, C., Bodhenheimer, H.C., Jr., Parés, A., et al. (2015). Efficacy of obeticholic acid in patients with primary biliary cirrhosis and inadequate response to ursodeoxycholic acid. Gastroenterology *148*, 751–61.e8. https://doi.org/10.1053/j.gastro.2014.12.005.

23. Kowdley, K.V., Luketic, V., Chapman, R., Hirschfield, G.M., Poupon, R., Schramm, C., Vincent, C., Rust, C., Parés, A., Mason, A., et al. (2018). A randomized trial of obeticholic acid monotherapy in patients with primary biliary cholangitis. Hepatology *67*, 1890–1902. https://doi.org/10.1002/hep.29569.

24. Nevens, F., Andreone, P., Mazzella, G., Strasser, S.I., Bowlus, C., Invernizzi, P., Drenth, J.P.H., Pockros, P.J., Regula, J., Beuers, U., et al. (2016). A Placebo-Controlled Trial of Obeticholic Acid in Primary Biliary Cholangitis. N. Engl. J. Med. *375*, 631–643. https://doi.org/10.1056/NEJMoa1509840.

25. Neuschwander-Tetri, B.A., Loomba, R., Sanyal, A.J., Lavine, J.E., Van Natta, M.L., Abdelmalek, M.F., Chalasani, N., Dasarathy, S., Diehl, A.M., Hameed, B., et al. (2015). Farnesoid X nuclear receptor ligand obeticholic acid for non-cirrhotic, non-alcoholic steatohepatitis (FLINT): a multicentre, randomised, placebo-controlled trial. Lancet *385*, 956–965. https://doi.org/10.1016/S0140-6736(14)61933-4.

26. Hameed, B., Terrault, N.A., Gill, R.M., Loomba, R., Chalasani, N., Hoofnagle, J.H., and Van Natta, M.L. (2018). Clinical and metabolic effects associated with weight changes and obeticholic acid in non-alcoholic steatohepatitis. Aliment. Pharmacol. Ther. *47*, 645–656. https://doi.org/10.1111/apt.14492.

27. Younossi, Z.M., Ratziu, V., Loomba, R., Rinella, M., Anstee, Q.M., Goodman, Z., Bedossa, P., Geier, A., Beckebaum, S., Newsome, P.N., et al. (2019). Obeticholic acid for the treatment of non-alcoholic steatohepatitis: interim analysis from a multicentre, randomised, placebo-controlled phase 3 trial. Lancet *394*, 2184–2196. https://doi.org/10.1016/S0140-6736(19)33041-7.

28. Roberts, S.B., Ismail, M., Kanagalingam, G., Mason, A.L., Swain, M.G., Vincent, C., Yoshida, E.M., Tsien, C., Flemming, J.A., Janssen, H.L.A., et al. (2020). Real-World Effectiveness of Obeticholic Acid in Patients with Primary Biliary Cholangitis. Hepatol. Commun. *4*, 1332–1345. https://doi.org/10.1002/hep4.1518.

29. D'Amato, D., De Vincentis, A., Malinverno, F., Viganò, M., Alvaro, D., Pompili, M., Picciotto, A., Palitti, V.P., Russello, M., Storato, S., et al. (2021). Real-world experience with obeticholic acid in patients with primary biliary cholangitis. JHEP Rep. *3*, 100248. https://doi.org/10.1016/j.jhepr.2021.100248.

30. Kowdley, K.V., Vuppalanchi, R., Levy, C., Floreani, A., Andreone, P., LaRusso, N.F., Shrestha, R., Trotter, J., Goldberg, D., Rushbrook, S., et al. (2020). A randomized, placebo-controlled, phase II study of obeticholic acid for primary sclerosing cholangitis. J. Hepatol. *73*, 94–101. https://doi.org/10.1016/j.jhep.2020.02.033.

31. Younossi, Z.M., Stepanova, M., Nader, F., Loomba, R., Anstee, Q.M., Ratziu, V., Harrison, S., Sanyal, A.J., Schattenberg, J.M., Barritt, A.S., et al. (2022). Obeticholic Acid Impact on Quality of Life in Patients With Nonalcoholic Steatohepatitis: REGENERATE 18-Month Interim Analysis. Clin. Gastroenterol. Hepatol. *20*, 2050–2058.e12. https://doi.org/10.1016/j.cgh.2021.07.020.

32. Neuschwander-Tetri, B., Sanyal, A., Loomba, R., Chalasani, N., Kowdley, K., Abdelmalek, M., Brunt, E., and Shapiro, D. (2015). LP18: Obeticholic acid for NASH: benefits in a high risk subgroup and the effects of concomitant statin use. J. Hepatol. *62*, S272. https://doi.org/10.1016/S0168-8278(15)30172-0.

33. Pockros, P.J., Fuchs, M., Freilich, B., Schiff, E., Kohli, A., Lawitz, E.J., Hellstern, P.A., Owens-Grillo, J., Van Biene, C., Shringarpure, R., et al. (2019). CONTROL: A randomized phase 2 study of obeticholic acid and atorvastatin on lipoproteins in nonalcoholic steatohepatitis patients. Liver Int. *39*, 2082–2093. https://doi.org/10.1111/liv.14209.

34. Chiang, J.Y.L. (2009). Bile acids: regulation of synthesis. J. Lipid Res. *50*, 1955–1966. https://doi.org/10.1194/jlr.R900010-JLR200.

35. Li, T., and Chiang, J.Y.L. (2014). Bile acid signaling in metabolic disease and drug therapy. Pharmacol. Rev. *66*, 948–983. https://doi.org/10.1124/pr.113.008201.

36. Zi, Z.T., and Rao, Y. (2024). Discoveries of GPR39 as an evolutionarily conserved receptor for bile acids and of its involvement in biliary acute pancreatitis. Sci. Adv. *10*, eadj0146. https://doi.org/10.1126/sciadv.adj0146.

37. Zhuang, S.T., Li, Q., Cai, L.R., Wang, C., and Lei, X.G. (2017). Chemoproteomic Profiling of Bile Acid Interacting Proteins. ACS Cent. Sci. *3*, 501–509. https://doi.org/10.1021/acscentsci.7b00134.

38. Mohanty, I., Mannochio-Russo, H., Schweer, J.V., El Abiead, Y., Bittremieux, W., Xing, S., Schmid, R., Zuffa, S., Vasquez, F., Muti, V.B., et al. (2024). The underappreciated diversity of bile acid modifications. Cell *187*, 1801–1818.e20. https://doi.org/10.1016/j.cell.2024.02.019.

39. Yu, H., Wangensteen, K., Deng, T., Li, Y., and Luo, W. (2021). MRGPRX4 in Cholestatic Pruritus. Semin. Liver Dis. *41*, 358–367. https://doi.org/10.1055/s-0041-1730923.

40. Beuers, U., Wolters, F., and Oude Elferink, R.P.J. (2023). Mechanisms of pruritus in cholestasis: understanding and treating the itch. Nat. Rev. Gastroenterol. Hepatol. *20*, 26–36. https://doi.org/10.1038/s41575-022-00687-7.

41. Nietsche, T.R., Dotta, G., Barcaui, C.B., and Ferraz, M.L.C.G. (2022). Cholestatic pruritus: a knowledge update. An. Bras. Dermatol. *97*, 332–337. https://doi.org/10.1016/j.abd.2021.06.007.

42. Mittal, A. (2016). Cholestatic Itch Management. Curr. Probl. Dermatol. *50*, 142–148. https://doi.org/10.1159/000446057.

43. Kremer, A.E., Bolier, R., van Dijk, R., Oude Elferink, R.P.J., and Beuers, U. (2014). Advances in pathogenesis and management of pruritus in cholestasis. Dig. Dis. *32*, 637–645. https://doi.org/10.1159/000360518.

44. Düll, M.M., and Kremer, A.E. (2019). Treatment of Pruritus Secondary to Liver Disease. Curr. Gastroenterol. Rep. *21*, 48. https://doi.org/10.1007/s11894-019-0713-6.

45. Prince, M.I., Burt, A.D., and Jones, D.E. (2002). Hepatitis and liver dysfunction with rifampicin therapy for pruritus in primary biliary cirrhosis. Gut *50*, 436–439. https://doi.org/10.1136/gut.50.3.436.

46. Beuers, U. (2006). Drug insight: Mechanisms and sites of action of ursodeoxycholic acid in cholestasis. Nat. Clin. Pract. Gastroenterol. Hepatol. *3*, 318–328. https://doi.org/10.1038/ncpgasthep0521.

47. Rust, C., Sauter, G.H., Oswald, M., Büttner, J., Kullak-Ublick, G.A., Paumgartner, G., and Beuers, U. (2000). Effect of cholestyramine on bile acid pattern and synthesis during administration of ursodeoxycholic acid in man. Eur. J. Clin. Invest. *30*, 135–139. https://doi.org/10.1046/j.1365-2362.2000.00606.x.

48. Corpechot, C., Chazouillères, O., Rousseau, A., Le Gruyer, A., Habersetzer, F., Mathurin, P., Goria, O., Potier, P., Minello, A., Silvain, C., et al. (2018). A Placebo-Controlled Trial of Bezafibrate in Primary Biliary Cholangitis. N. Engl. J. Med. *378*, 2171–2181. https://doi.org/10.1056/NEJMoa1714519.

49. Liu, T., Wang, R.X., Han, J., Hao, C.Z., Qiu, Y.L., Yan, Y.Y., Li, L.T., Wang, N.L., Gong, J.Y., Lu, Y., et al. (2018). Comprehensive bile acid profiling in hereditary intrahepatic cholestasis: Genetic and clinical correlations. Liver Int. *38*, 1676–1685. https://doi.org/10.1111/liv.13714.

50. Kato, T., Yoneda, M., Nakamura, K., and Makino, I. (1996). Enzymatic determination of serum 3 alpha-sulfated bile acids concentration with bile acid 3 alpha-sulfate sulfohydrolase. Dig. Dis. Sci. *41*, 1564–1570. https://doi.org/10.1007/BF02087901.

51. Baumann, U., Sturm, E., Lacaille, F., Gonzalès, E., Arnell, H., Fischler, B., Jørgensen, M.H., Thompson, R.J., Mattsson, J.P., Ekelund, M., et al. (2021). Effects of odevixibat on pruritus and bile acids in children with cholestatic liver disease: Phase 2 study. Clin. Res. Hepatol. Gastroenterol. *45*, 101751. https://doi.org/10.1016/j.clinre.2021.101751.

52. Yu, H., Zhao, T., Liu, S., Wu, Q., Johnson, O., Wu, Z., Zhuang, Z., Shi, Y., Peng, L., He, R., et al. (2019). MRGPRX4 is a bile acid receptor for human cholestatic itch. eLife *8*, e48431. https://doi.org/10.7554/eLife.48431.

53. Al Hamwi, G., Riedel, Y.K., Clemens, S., Namasivayam, V., Thimm, D., and Müller, C.E. (2022). MAS-related G protein-coupled receptors X (MRGPRX): orphan GPCRs with potential as targets for future drugs. Pharmacol. Ther. *238*, 108259. https://doi.org/10.1016/j.pharmthera.2022.108259.

54. Dong, X., Han, S., Zylka, M.J., Simon, M.I., and Anderson, D.J. (2001). A diverse family of GPCRs expressed in specific subsets of nociceptive sensory neurons. Cell *106*, 619–632. https://doi.org/10.1016/s0092-8674(01)00483-4.

55. Meixiong, J., Vasavda, C., Snyder, S.H., and Dong, X. (2019). MRGPRX4 is a G protein-coupled receptor activated by bile acids that may contribute to cholestatic pruritus. Proc. Natl. Acad. Sci. USA *116*, 10525–10530. https://doi.org/10.1073/pnas.1903316116.

56. Tazawa, Y., Yamada, M., Nakagawa, M., Konno, Y., and Tada, K. (1984). Unconjugated, glycine-conjugated, taurine-conjugated bile acid nonsulfates and sulfates in urine of young infants with cholestasis. Acta Paediatr. Scand. *73*, 392–397. https://doi.org/10.1111/j.1651-2227.1994.tb17754.x.

57. Makino, I., Hashimoto, H., Shinozaki, K., Yoshino, K., and Nakagawa, S. (1975). Sulfated and nonsulfated bile acids in urine, serum, and bile of patients with hepatobiliary diseases. Gastroenterology *68*, 545–553. https://doi.org/10.1016/S0016-5085(75)80094-1.

58. Li, Y., Zhang, X., Chen, J., Feng, C., He, Y., Shao, Y., and Ding, M. (2018). Targeted metabolomics of sulfated bile acids in urine for the diagnosis and grading of intrahepatic cholestasis of pregnancy. Genes Dis. *5*, 358–366. https://doi.org/10.1016/j.gendis.2018.01.005.

59. Alnouti, Y. (2009). Bile Acid sulfation: a pathway of bile acid elimination and detoxification. Toxicol. Sci. *108*, 225–246. https://doi.org/10.1093/toxsci/kfn268.

60. Yao, L., D'Agostino, G.D., Park, J., Hang, S., Adhikari, A.A., Zhang, Y., Li, W., Avila-Pacheco, J., Bae, S., Clish, C.B., et al. (2022). A biosynthetic pathway for the selective sulfonation of steroidal metabolites by human gut bacteria. Nat. Microbiol. *7*, 1404–1418. https://doi.org/10.1038/s41564-022-01176-y.

61. Stiehl, A., Becker, M., Czygan, P., Fröhling, W., Kommerell, B., Rothauwe, H.W., and Senn, M. (1980). Bile acids and their sulphated and glucuronidated derivatives in bile, plasma, and urine of children with intrahepatic cholestasis: effects of phenobarbital treatment. Eur. J. Clin. Invest. *10*, 307–316. https://doi.org/10.1111/j.1365-2362.1980.tb00038.x.

62. Dong, X., and Dong, X. (2018). Peripheral and central mechanisms of itch. Neuron *98*, 482–494. https://doi.org/10.1016/j.neuron.2018.03.023.

63. Chen, X.J., and Sun, Y.G. (2020). Central circuit mechanisms of itch. Nat. Commun. *11*, 3052. https://doi.org/10.1038/s41467-020-16859-5.

64. Zylka, M.J., Dong, X., Southwell, A.L., and Anderson, D.J. (2003). Atypical expansion in mice of the sensory neuron-specific Mrg G protein-coupled receptor family. Proc. Natl. Acad. Sci. USA *100*, 10043–10048. https://doi.org/10.1073/pnas.1732949100.

65. Liu, Q., Tang, Z., Surdenikova, L., Kim, S., Patel, K.N., Kim, A., Ru, F., Guan, Y., Weng, H.J., Geng, Y., et al. (2009). Sensory neuron-specific GPCR Mrgprs are itch receptors mediating chloroquine-induced pruritus. Cell *139*, 1353–1365. https://doi.org/10.1016/j.cell.2009.11.034.

66. Cao, C., Kang, H.J., Singh, I., Chen, H., Zhang, C., Ye, W., Hayes, B.W., Liu, J., Gumpper, R.H., Bender, B.J., et al. (2021). Structure, function and pharmacology of human itch GPCRs. Nature *600*, 170–175. https://doi.org/10.1038/s41586-021-04126-6.

67. Chien, D.C.C., Limjunyawong, N., Cao, C., Meixiong, J., Peng, Q., Ho, C.Y., Fay, J.F., Roth, B.L., and Dong, X. (2024). MRGPRX4 mediates phospho-drug–associated pruritus in a humanized mouse model. Sci. Transl. Med. *16*, eadk8198. https://doi.org/10.1126/scitranslmed.adk8198.

68. Marx, D., Alnouri, M.W., Clemens, S., Gedschold, R., Riedel, Y., Al Hamwi, G., Pillaiyar, T., Hockemeyer, J., Namasivayam, V., and Müller, C.E. (2023). Discovery of Potent Agonists for the Predominant Variant of the Orphan MAS-Related G Protein-Coupled Receptor X4 (MRGPRX4). J. Med. Chem. *66*, 15674–15698. https://doi.org/10.1021/acs.jmedchem.3c01013.

69. Guo, L., Zhang, Y., Fang, G., Tie, L., Zhuang, Y., Xue, C., Liu, Q., Zhang, M., Zhu, K., You, C., et al. (2023). Ligand recognition and G protein coupling of the human itch receptor MRGPRX1. Nat. Commun. *14*, 5004. https://doi.org/10.1038/s41467-023-40705-z.

70. Liu, Y., Cao, C., Huang, X.P., Gumpper, R.H., Rachman, M.M., Shih, S.L., Krumm, B.E., Zhang, S., Shoichet, B.K., Fay, J.F., and Roth, B.L. (2023). Ligand recognition and allosteric modulation of the human MRGPRX1 receptor. Nat. Chem. Biol. *19*, 416–422. https://doi.org/10.1038/s41589-022-01173-6.

71. Yang, F., Guo, L., Li, Y., Wang, G., Wang, J., Zhang, C., Fang, G.X., Chen, X., Liu, L., Yan, X., et al. (2021). Structure, function and pharmacology of human itch receptor complexes. Nature *600*, 164–169. https://doi.org/10.1038/s41586-021-04077-y.

72. Kim, K., Che, T., Panova, O., DiBerto, J.F., Lyu, J., Krumm, B.E., Wacker, D., Robertson, M.J., Seven, A.B., Nichols, D.E., et al. (2020). Structure of

a Hallucinogen-Activated Gq-Coupled 5-HT(2A) Serotonin Receptor. Cell *182*, 1574–1588.e19. https://doi.org/10.1016/j.cell.2020.08.024.

73. Carpenter, B., Nehmé, R., Warne, T., Leslie, A.G.W., and Tate, C.G. (2016). Structure of the adenosine A(2A) receptor bound to an engineered G protein. Nature *536*, 104–107. https://doi.org/10.1038/nature18966.
74. Rasmussen, S.G.F., DeVree, B.T., Zou, Y., Kruse, A.C., Chung, K.Y., Kobilka, T.S., Thian, F.S., Chae, P.S., Pardon, E., Calinski, D., et al. (2011). Crystal structure of the β2 adrenergic receptor-Gs protein complex. Nature *477*, 549–555. https://doi.org/10.1038/nature10361.
75. Varadi, D.P. (1974). Pruritus induced by crude bile and purified bile acids. Experimental production of pruritus in human skin. Arch. Dermatol. *109*, 678–681. https://doi.org/10.1001/archderm.1974.01630050024005.
76. Kirby, J., Heaton, K.W., and Burton, J.L. (1974). Pruritic effect of bile salts. Br. Med. J. *4*, 693–695. https://doi.org/10.1136/bmj.4.5946.693.
77. Tully, D.C., Rucker, P.V., Chianelli, D., Williams, J., Vidal, A., Alper, P.B., Mutnick, D., Bursulaya, B., Schmeits, J., Wu, X., et al. (2017). Discovery of Tropifexor (LJN452), a Highly Potent Non-bile Acid FXR Agonist for the Treatment of Cholestatic Liver Diseases and Nonalcoholic Steatohepatitis (NASH). J. Med. Chem. *60*, 9960–9973. https://doi.org/10.1021/acs.jmedchem.7b00907.
78. Pedrosa, M., Seyedkazemi, S., Francque, S., Sanyal, A., Rinella, M., Charlton, M., Loomba, R., Ratziu, V., Kochuparampil, J., Fischer, L., et al. (2020). A randomized, double-blind, multicenter, phase 2b study to evaluate the safety and efficacy of a combination of tropifexor and cenicriviroc in patients with nonalcoholic steatohepatitis and liver fibrosis: Study design of the TANDEM trial. Contemp. Clin. Trials *88*, 105889. https://doi.org/10.1016/j.cct.2019.105889.
79. Forman, B.M., Goode, E., Chen, J., Oro, A.E., Bradley, D.J., Perlmann, T., Noonan, D.J., Burka, L.T., McMorris, T., Lamph, W.W., et al. (1995). Identification of a nuclear receptor that is activated by farnesol metabolites. Cell *81*, 687–693. https://doi.org/10.1016/0092-8674(95)90530-8.
80. Pellicciari, R., Gioiello, A., Macchiarulo, A., Thomas, C., Rosatelli, E., Natalini, B., Sardella, R., Pruzanski, M., Roda, A., Pastorini, E., et al. (2009). Discovery of 6α-Ethyl-23(S)-methylcholic Acid (S-EMCA, INT-777) as a Potent and Selective Agonist for the TGR5 Receptor, a Novel Target for Diabesity. J. Med. Chem. *52*, 7958–7961. https://doi.org/10.1021/jm901390p.
81. Mi, L.Z., Devarakonda, S., Harp, J.M., Han, Q., Pellicciari, R., Willson, T.M., Khorasanizadeh, S., and Rastinejad, F. (2003). Structural Basis for Bile Acid Binding and Activation of the Nuclear Receptor FXR. Mol. Cell *11*, 1093–1100. https://doi.org/10.1016/S1097-2765(03)00112-6.
82. Claudel, T., Staels, B., and Kuipers, F. (2005). The Farnesoid X receptor: a molecular link between bile acid and lipid and glucose metabolism. Arterioscler. Thromb. Vasc. Biol. *25*, 2020–2030. https://doi.org/10.1161/01.ATV.0000178994.21828.a7.
83. Orsler, D.J., Ahmed-Choudhury, J., Chipman, J.K., Hammond, T., and Coleman, R. (1999). ANIT-induced disruption of biliary function in rat hepatocyte couplets. Toxicol. Sci. *47*, 203–210. https://doi.org/10.1093/toxsci/47.2.203.
84. Canbay, A., Higuchi, H., Bronk, S.F., Taniai, M., Sebo, T.J., and Gores, G.J. (2002). Fas enhances fibrogenesis in the bile duct ligated mouse: A link between apoptosis and fibrosis. Gastroenterology *123*, 1323–1330. https://doi.org/10.1053/gast.2002.35953.
85. Wallace, M.C., Hamesch, K., Lunova, M., Kim, Y., Weiskirchen, R., Strnad, P., and Friedman, S.L. (2015). Standard operating procedures in experimental liver research: thioacetamide model in mice and rats. Lab. Anim. *49*, 21–29. https://doi.org/10.1177/0023677215573040.
86. Watanabe, M., Houten, S.M., Wang, L., Moschetta, A., Mangelsdorf, D.J., Heyman, R.A., Moore, D.D., and Auwerx, J. (2004). Bile acids lower triglyceride levels via a pathway involving FXR, SHP, and SREBP-1c. J. Clin. Invest. *113*, 1408–1418. https://doi.org/10.1172/JCI21025.
87. Mustafa, H.N., El Awdan, S.A., and Hegazy, G.A. (2013). Protective role of antioxidants on thioacetamide-induced acute hepatic encephalopathy: biochemical and ultrastructural study. Tissue Cell *45*, 350–362. https://doi.org/10.1016/j.tice.2013.06.001.
88. Patel, K., Harrison, S.A., Elkhashab, M., Trotter, J.F., Herring, R., Rojter, S.E., Kayali, Z., Wong, V.W.S., Greenbloom, S., Jayakumar, S., et al. (2020). Cilofexor, a Nonsteroidal FXR Agonist, in Patients With Noncirrhotic NASH: A Phase 2 Randomized Controlled Trial. Hepatology *72*, 58–71. https://doi.org/10.1002/hep.31205.
89. Harrison, S.A., Bashir, M.R., Lee, K.J., Shim-Lopez, J., Lee, J., Wagner, B., Smith, N.D., Chen, H.C., and Lawitz, E.J. (2021). A structurally optimized FXR agonist, MET409, reduced liver fat content over 12 weeks in patients with non-alcoholic steatohepatitis. J. Hepatol. *75*, 25–33. https://doi.org/10.1016/j.jhep.2021.01.047.
90. Day, C.P., and James, O.F. (1998). Steatohepatitis: a tale of two "hits"? Gastroenterology *114*, 842–845. https://doi.org/10.1016/s0016-5085(98)70599-2.
91. Buzzetti, E., Pinzani, M., and Tsochatzis, E.A. (2016). The multiple-hit pathogenesis of non-alcoholic fatty liver disease (NAFLD). Metabolism *65*, 1038–1048. https://doi.org/10.1016/j.metabol.2015.12.012.
92. Van Herck, M.A., Vonghia, L., and Francque, S.M. (2017). Animal Models of Nonalcoholic Fatty Liver Disease-A Starter's Guide. Nutrients *9*, 1072. https://doi.org/10.3390/nu9101072.
93. Wei, E., Ben Ali, Y., Lyon, J., Wang, H., Nelson, R., Dolinsky, V.W., Dyck, J.R.B., Mitchell, G., Korbutt, G.S., and Lehner, R. (2010). Loss of TGH/Ces3 in mice decreases blood lipids, improves glucose tolerance, and increases energy expenditure. Cell Metab. *11*, 183–193. https://doi.org/10.1016/j.cmet.2010.02.005.
94. Kim, S.H., Lim, Y., Park, J.B., Kwak, J.H., Kim, K.J., Kim, J.H., Song, H., Cho, J.Y., Hwang, D.Y., Kim, K.S., and Jung, Y.S. (2017). Comparative study of fatty liver induced by methionine and choline-deficiency in C57BL/6N mice originating from three different sources. Lab. Anim. Res. *33*, 157–164. https://doi.org/10.5625/lar.2017.33.2.157.
95. Sepe, V., Festa, C., Renga, B., Carino, A., Cipriani, S., Finamore, C., Masullo, D., Del Gaudio, F., Monti, M.C., Fiorucci, S., and Zampella, A. (2016). Insights on FXR selective modulation. Speculation on bile acid chemical space in the discovery of potent and selective agonists. Sci. Rep. *6*, 19008. https://doi.org/10.1038/srep19008.
96. Xiao, H., Li, P., Li, X., He, H., Wang, J., Guo, F., Zhang, J., Wei, L., Zhang, H., Shi, Y., et al. (2017). Synthesis and Biological Evaluation of a Series of Bile Acid Derivatives as FXR Agonists for Treatment of NASH. ACS Med. Chem. Lett. *8*, 1246–1251. https://doi.org/10.1021/acsmedchemlett.7b00318.
97. Ratziu, V., Rinella, M.E., Neuschwander-Tetri, B.A., Lawitz, E., Denham, D., Kayali, Z., Sheikh, A., Kowdley, K.V., Desta, T., Elkhashab, M., et al. (2022). EDP-305 in patients with NASH: A phase II double-blind placebo-controlled dose-ranging study. J. Hepatol. *76*, 506–517. https://doi.org/10.1016/j.jhep.2021.10.018.
98. Zivanov, J., Nakane, T., Forsberg, B.O., Kimanius, D., Hagen, W.J., Lindahl, E., and Scheres, S.H. (2018). New tools for automated high-resolution cryo-EM structure determination in RELION-3. eLife *7*, e42166. https://doi.org/10.7554/eLife.42166.
99. Punjani, A., Rubinstein, J.L., Fleet, D.J., and Brubaker, M.A. (2017). cryoSPARC: algorithms for rapid unsupervised cryo-EM structure determination. Nat. Methods *14*, 290–296. https://doi.org/10.1038/nmeth.4169.
100. Pettersen, E.F., Goddard, T.D., Huang, C.C., Couch, G.S., Greenblatt, D.M., Meng, E.C., and Ferrin, T.E. (2004). UCSF Chimera–a visualization system for exploratory research and analysis. J. Comput. Chem. *25*, 1605–1612. https://doi.org/10.1002/jcc.20084.
101. Emsley, P., and Cowtan, K. (2004). Coot: model-building tools for molecular graphics. Acta Crystallogr. D Biol. Crystallogr. *60*, 2126–2132. https://doi.org/10.1107/S0907444904019158.
102. Adams, P.D., Afonine, P.V., Bunkóczi, G., Chen, V.B., Davis, I.W., Echols, N., Headd, J.J., Hung, L.W., Kapral, G.J., Grosse-Kunstleve, R.W., et al. (2010). Phenix: a comprehensive Python-based system for

macromolecular structure solution. Acta Crystallogr. D Biol. Crystallogr. *66*, 213–221. https://doi.org/10.1107/S0907444909052925.

103. Zheng, S.Q., Palovcak, E., Armache, J.P., Verba, K.A., Cheng, Y., and Agard, D.A. (2017). MotionCor2: anisotropic correction of beam-induced motion for improved cryo-electron microscopy. Nat. Methods *14*, 331–332. https://doi.org/10.1038/nmeth.4193.

104. Zhang, K. (2016). Gctf: Real-time CTF determination and correction. J. Struct. Biol. *193*, 1–12. https://doi.org/10.1016/j.jsb.2015.11.003.

105. Xiang, X., Han, Y., Neuvonen, M., Laitila, J., Neuvonen, P.J., and Niemi, M. (2010). High performance liquid chromatography-tandem mass spectrometry for the determination of bile acid concentrations in human plasma. J. Chromatogr. B Analyt. Technol. Biomed. Life Sci. *878*, 51–60. https://doi.org/10.1016/j.jchromb.2009.11.019.

106. Zhao, Z.Q., Liu, X.Y., Jeffry, J., Karunarathne, W.K.A., Li, J.L., Munanairi, A., Zhou, X.Y., Li, H., Sun, Y.G., Wan, L., et al. (2014). Descending control of itch transmission by the serotonergic system via 5-HT1A-facilitated GRP-GRPR signaling. Neuron *84*, 821–834. https://doi.org/10.1016/j.neuron.2014.10.003.

107. Sun, Y.G., and Chen, Z.F. (2007). A gastrin-releasing peptide receptor mediates the itch sensation in the spinal cord. Nature *448*, 700–703. https://doi.org/10.1038/nature06029.

108. Sun, Y.G., Zhao, Z.Q., Meng, X.L., Yin, J., Liu, X.Y., and Chen, Z.F. (2009). Cellular basis of itch sensation. Science *325*, 1531–1534. https://doi.org/10.1126/science.1174868.

109. Thomsen, J.S., Petersen, M.B., Benfeldt, E., Jensen, S.B., and Serup, J. (2001). Scratch induction in the rat by intradermal serotonin: a model for pruritus. Acta Derm. Venereol. *81*, 250–254. https://doi.org/10.1080/00015550152572868.

110. Tag, C.G., Weiskirchen, S., Hittatiya, K., Tacke, F., Tolba, R.H., and Weiskirchen, R. (2015). Induction of experimental obstructive cholestasis in mice. Lab. Anim. *49*, 70–80. https://doi.org/10.1177/0023677214567748.

Please cite this article in press as: Yang et al., Structure-guided discovery of bile acid derivatives for treating liver diseases without causing itch, Cell (2024), https://doi.org/10.1016/j.cell.2024.10.001

STAR★METHODS

KEY RESOURCES TABLE

REAGENT or RESOURCE	SOURCE	IDENTIFIER
Bacterial and virus strains		
Escherichia coli DH5α	ZOMANBIO	Cat#ZC101-1
Escherichia coli DH10bac	ZOMANBIO	Cat#ZC1020-1
Chemicals, peptides, and recombinant proteins		
Apyrase	NEB	Cat#M0398L
Lauryl maltose neopentyl glycerol (LMNG)	Anatrace	Cat#NG310
Cholesteryl hemisuccinate (CHS)	Anatrace	Cat#CH210
Poly-L-lysine	Sigma	Cat#P2636
Sf-900 II SFM	Invitrogen	Cat#10902096
DCA	HARVEYBIO	Cat#SR1497
DCA-3S	This paper	N/A
DCA-3P	This paper	N/A
OCA	HARVEYBIO	Cat#SR4579
OCA-3S	This paper	N/A
OCA-3P	This paper	N/A
C7	This paper	N/A
scFv16	This paper	N/A
Fluo-8 AM	AAT Bio.	CAT#AAT-21081
TEV enzyme	This paper	N/A
Critical commercial assays		
Bac-to-Bac Expression system	Invitrogen	Cat#A11100
ClonExpress II One Step Cloning Kit	Vazyme	Cat#C113-01
Deposited data		
Overall structure of hX4-Gq bound with DCA-3P	This paper	PDB ID: 8K4S
Structure of hX4 bound with DCA-3P, local refinement	This paper	PDB ID: 8KEX
The cryo-EM maps for hX4-Gq bound with DCA-3P	This paper	EMDB ID: EMD-36890
The local refinement maps of hX4 bound with DCA-3P	This paper	EMDB ID: EMD-37191
Experimental models: Cell lines		
HEK293T	ATCC	Cat#CRL-3216
Spodoptera frugiperda 9 (Sf9) cells	Expression Systems	Cat#94-001S
DRG neurons	This paper	N/A
HepG2	ATCC	Cat#KCSP.ATCC.HB-8065
Experimental models: Organisms/strains		
hX4-humanized rats	This paper	N/A
Rats	Charles River	N/A
Mice	Charles River	N/A
Oligonucleotides		
Primers list for qPCR	This paper	See Table S2
Recombinant DNA		
pFastBac-BrilX4	This paper	N/A
pFastBacDual-miniGαq-Gβ-Gγ	This paper	N/A
pIsecSUMOstar-scFv16	This paper	N/A

(*Continued on next page*)

Continued

REAGENT or RESOURCE	SOURCE	IDENTIFIER
piggyBac-hX4	This paper	N/A
Software and algorithms		
Relion 3.0	Kimanius et al.[98]	https://relion.readthedocs.io/en/release-4.0/Installation.html
cryoSPARC	Punjani et al.[99]	https://cryosparc.com/
UCSF Chimera	Pettersen et al.[100]	a
WinCoot 0.9.8.1	Emsley et al.[101]	https://bernhardcl.github.io/coot/wincoot-download.html
Phenix	Adams et al.[102]	https://phenix-online.org/
GraphPad Prism 9.0	Graphpad Software Inc.	https://www.graphpad.com/ RRID:SCR_002798
Other		
Superdex 200 Increase 10/300 column	GE healthcare	Cat#28990944
Strep-Tacin beads	Smart-Life-sciences	Cat#SA053025
Ni-NTA beads 6FF	Smart-Life-sciences	Cat#SA005100

EXPERIMENTAL MODEL AND STUDY PARTICIPANT DETAILS

Animals

All animals used in the study were purchased from Charles River Laboratories (Beijing, China). Male rats (4-6 weeks of age; 200-300 g) or male mice (2-3 months of age; 20-30 g) were used for all animal experiments. All animals were group-housed (3-5 animals per cage) under a standard 12-hour light/ 12-hour dark cycle, and all behavioral experiments were performed during the light cycle. All animal experiments were approved by the Animal Care and Use Committee of Peking University School of Life Sciences.

Human subjects

The human itch tests were approved by the Committee for Protecting Human and Animal Subjects at the Department of Psychology, Peking University. The volunteers were students and faculty members at Peking University. For cholestatic patients, the Ethics Committee of Beijing Youan Hospital Capital Medical University approved the collection of patients' plasma, and the information on these patients is shown in Data S1.

METHOD DETAILS

General

Primers were synthesized in Xianghong Co. Ltd., and genes were synthesized in Generay Co. Ltd. DNA sequencing was performed by RuiBiotech Company. ClonExpress II One Step Cloning Kit was purchased from Vazyme Biotech. PCR was carried out to obtain DNA fragments using standard thermal cycling protocols with TransStart FastPfu DNA polymerase (Transgene Biotech). Plasmid piggy-X4 was used to construct cell lines that stably express hX4 in the same way as in the previous study.[52]

Chemistry

^{1}H NMR spectra were recorded on Bruker 400 MHz spectrometers at ambient temperature with $CDCl_3$, methanol-d_4, or DMSO-d_6 as the solvent unless otherwise stated. ^{13}C NMR spectra were recorded at ambient temperature on a Brucker 100 MHz spectrometer (with complete proton decoupling). Chemical shifts are reported in parts per million relatives to $CDCl_3$, methanol-d_4 or DMSO-d_6 (^{1}H, δ 7.26 for $CDCl_3$, 3.31 for methanol-d_4, 2.50 for DMSO-d_6; ^{13}C, δ 77.16 for $CDCl_3$, 49.00 for methanol-d_4, 39.52 for DMSO-d_6). Data for ^{1}H NMR are reported as follows: chemical shift, integration, multiplicity (s = singlet, d = doublet, t = triplet, dd = doublet of doublets, m = multiplet), and coupling constants. Peking University Mass Spectrometry Laboratory used Bruker APEX Flash chromatography to obtain high-resolution mass spectra. Analytical thin-layer chromatography was performed using 0.25 mm silica gel 60-F plates. Flash chromatography was performed using 200-300 mesh silica gel. Yields refer to chromatographically and spectroscopically pure materials unless otherwise stated. Before use, tetrahydrofuran was distilled from sodium/benzophenone ketyl; the other solvents were distilled from calcium hydride unless otherwise noted. Reagents were purchased at the highest commercial quality and used without further purification unless otherwise stated. Unless otherwise noted, all reactions were carried out in oven-dried glassware under an argon atmosphere with dry solvents. The detailed procedures are shown in Methods S1.

Plasmid construction

For protein expression of hX4 in insect cell Sf9, the gene for human hX4 (UniProtKB-Q96LA9) was cloned into a modified pFastBac1-HA vector, which contains an N-terminal hemagglutinin signal peptide (HA-tag) followed by a flag-tag. To facilitate the expression of hX4, an apocytochrome b562RIL (BRIL) was inserted before the N-terminal of hX4. A HRV3C protease (ppase) site and the gene for GFP followed by a strep tag were introduced at the C-terminal of hX4 for further protein purification to generate plasmid pFastBac-BrilX4 (Data S2). We used the same miniGαq heterotrimer construct for the G protein construct as the previous studies.[66,71] The genes for $G_{\gamma 1}$-fused miniGαq and $G_{\beta 1}$ were introduced after the p10 and polyhedrin promotor of the pFastBacDual vector, respectively (Data S2). For expression of scFv16, the gene of scFv16 was obtained by PCR using a synthesized gene as a template with Fastpfu polymerase (TransGene). Linear pI-secSUMOstar vector was obtained by PCR. A ClonExpress II One Step Cloning Kit (Vazyme Biotech Co. Ltd) generated the plasmid pIsecSUMOstar-scFv16.

Expression and purification of scFv16

The expression and purification of scFv16 were performed as previously described with slight modification. Briefly, plasmid pIsecSUMOstar-scFv16 was transformed into *E. coli* DH10Bac competent cells to obtain bacmid containing the scFv16 gene. Generation and amplification of recombinant baculoviruses and protein expression were conducted in Sf9 insect cells. The cells were infected with the recombinant virus at a density of 2.5×10^6 with a ratio of 1:200 (virus: cells, v/v). Recombinant scFv16 was expressed as a secreted protein with N-terminal 6 × His and SUMO tags. The medium was harvested 60h after infection and concentrated using a Hydrosart Ultrafilter (Sartorius). Then, the medium was exchanged into buffer A (20 mM HEPES, 0.2M NaCl, pH 7.4). The crude protein was flowed through a gravity column containing Ni-NTA resin and washed with 20 column volumes of buffer A containing 15 mM imidazole. After this, scFv16 was eluted from the column with buffer A supplemented with 250mM imidazole and was exchanged into buffer A. Then, TEV enzymes were added to the sample and stored at 4°C overnight to remove 6 × His and SUMO tags. After digestion, the sample was flowed through Ni-NTA resin twice to remove TEV enzymes and 6 × His-SUMO tag. The sample in the flow-through was purified by size-exclusion chromatography using a Superdex increase of 200 10/300 GL (GE Healthcare) with buffer A. The peak fraction was collected and concentrated to 2 mg/ml for further use.

Expression of MRGPRX4-miniGαq protein complex

BRIL-fused MRGPRX4 with miniGαq and $G_{\beta 1}/G_{\gamma 2}$ were co-expressed in Sf9 cells. Two separate baculoviruses at a ratio of 4:2 for BRIL-MRGPRX4 and miniGαq/$G_{\beta 1}/G_{\gamma 2}$ co-infected Sf9 cells when they grow to a density of 3×10^6 cells per ml. After being infected for 48 hours at 27 °C, the cells were collected by centrifugation with 4000 rpm at 4 °C and the pellets were flash frozen with liquid nitrogen and then stored at -80 °C for further use.

Purification of MRGPRX4-miniGαq protein complex

Cell pellets expressing the MRGPRX4-miniGαq-$G_{\beta 1}/G_{\gamma 2}$ complex were resuspended in buffer containing 20 mM HEPES, 0.1 M NaCl, 5 mM $MgCl_2$, pH 7.5 supplemented with proteinase inhibitors and then 4 units of Apyase (NEB) was added into the buffer and incubated at room temperature. After incubation for an hour, the cell suspension was homogenized with a dounce homogenizer and followed by membranes collecting by centrifugation at 35000 × g for 30 min utilizing an SW32Ti rotor (Beckman). The membranes were resuspended in buffer containing 20 mM HEPES, 0.1 M NaCl, 5 mM $MgCl_2$, 5% (v/v) glycerol, pH 7.5 supplemented proteinase inhibitors and 1 unit of Apyase (NEB). After that, 0.6 % (w/v) lauryl maltose neopentyl glycol (LMNG), 0.06% (w/v) cholesteryl hemisuccinate (CHS), and 2 mg scFv16 were added into the suspension and rotated at 4 °C for 4 hours to solubilize membranes. The solubilized crude proteins were collected in the supernatants by ultracentrifugation at 45000 × g for 40 min using a SW32Ti rotor (Beckman) and flowed through the strep resin. The resin binding with MRGPRX4-miniGq complex was washed with 20 column volumes of wash buffer (20 mM HEPES, 0.1 M NaCl, pH 7.5, 0.01% (w/v) LMNG, and 0.001% CHS), and the protein was then eluted with 15 ml the same buffer supplemented with 1 mg/ml desthiobiotin (Thermol). The eluted protein was further purified with size-exclusion chromatography on a Superdex 200 Increase 10/300 column (GE Healthcare) pre-equilibrated with 20 mM HEPES, 0.1 M NaCl, 0.1 mM TCEP, 0.00075% (w/v) LMNG, 0.00075% (w/v) CHS and 0.00025% (w/v) glyco-diosgenin (GDN). Peak fractions were collected and concentrated to 5 mg/mL. After that, 200 μM DCA-3P was added to the protein and incubated at 4 °C for 2 h before grid-making. Notably, 10 μM DCA-3P was added to the buffer throughout the purification to stabilize the MRGPRX4-miniGq complex. The complex was confirmed by SDS-PAGE (Data S2).

Cryo-EM grid preparation and data collection

Verified samples were prepared by applying 3 μL purified proteins to glow-discharged gold grids (Quantifoil R1.2/1.3) individually and were flash frozen in liquid ethane cooled by liquid nitrogen utilizing a Vitrobot mark IV (FEI) set at 4 °C and 100% humidity. The blot time ranges from 1.5 to 3 s. Prepared grids were stored in liquid nitrogen for further use. The cryo-EM images were collected using an FEI Titan Krios electron microscope operating at an acceleration voltage of 300 kV and equipped with a K2 Summit direct electron detector (Gatan). Raw movies were automatically acquired in super-resolution mode with a physical pixel size of 1.04 Å using SerialEM. Each movie stack was recorded for 6.4 s fractionated into 32 frames with a total accumulated dose of ~60 e/ Å2. A total of 2,485 movie stacks were collected.

Three-dimensional reconstitution, model building and refinement

Drift and beam-induced motion corrections of all the original image stacks were conducted using MotionCor2.[103] The contrast transfer function (CTF) was estimated with Gctf.[104] A total of 1,537,700 particles were picked for 2D and 3D classification with a binning factor of two utilizing RELION-3.[98] The final best class was imported in cryoSPARC[99] and was refined to 2.91 Å. A local refinement for the receptor-only region was performed to improve the map quality. More details are shown in Data S2. The Gq trimer, scFv16, and MRGPRX4 complex were docked into the cryo-EM map with MRGPRX4-miniGq (PDB ID: 7S8P) as a template using UCSF Chimera.[100] The model of the MRGPRX4-miniGq complex was manually built in Coot,[101] followed by several rounds of real-space refinement with Phenix.[102] The ligand DCA-3P was fitted into the cryo-EM using Coot and refined with Phenix. The Cryo-EM data collection, model refinement, and validation statistics are shown in Data S2.

All-atom molecular dynamics simulations

CHARMM-GUI was used to generate the system, the POPC was utilized to build the phospholipid bilayer, and the concentration of NaCl was set to 0.15 M. The ff14SB force field, the gaff force field, the TIP3P model, and the lipid14 force field parameter were used for protein, ligands, water, and lipid, respectively, with the Leap module of the AmberTools21. We used AM1-BCC to assign the partial charge of the atoms in ligands. Long-range electrostatic effects were modeled using the particle mesh Ewald method with periodic boundary conditions. A 10 Å cut-off was applied to Lennard-Jones and electrostatic interactions. Molecular dynamics simulations were performed in the following steps: (1) Minimization for waters and lipids was performed with a maximum cycle of 10,000 and with the steepest descent algorithm for the first 5,000 cycles with the SHAKE algorithm (an algorithm for constrained molecular dynamics) inactivated. Positional restraints of 0.5 kcal/mol•Å^2 were applied to the protein and ligands. (2) Minimization for the whole system was performed with a maximum cycle of 10,000, and the steepest descent algorithm was used for the first 5,000 cycles, with the SHAKE algorithm inactivated. (3) A 1 ns Heating process was performed with a periodic boundary for constant volume with the SHAKE algorithm activated. Thus, the angle between the hydrogen atoms was fixed. The temperature increased from 0 K to 303 K with Langevin dynamics with a collision frequency of 2 ps^{-1}. (4) A 1 ns density equilibrium process was performed with a periodic boundary for constant pressure with anisotropic pressure scaling and a constant temperature of 303 K. (5) A 300 ns equilibrium process was performed with a periodic boundary for constant pressure and constant temperature of 303 K. Three independent dynamic simulations were performed for each complex structure. The analysis of the trajectory was done by Chimera1.15.[100]

MM/GBSA binding free energy calculation

Trajectory sampled by MD simulations were used for MM/GBSA binding affinity calculations and decompositions in the Amber20 program. All reported binding affinities and the decomposed components were averaged over 3 independent 200 ns MD trajectories (from 100 to 300 ns, 1 sample per ns). Entropic contributions were not calculated.

Plasma sample preparation and analysis of bile acids

Plasma from patients was separated from blood by routine centrifugation. 50 μL plasmas were used for bile acids analysis using an Agilent 1260-6495 LC-MS/MS system equipped with an electrospray ionization source with an HSS T3 column (Waters; 2.1 mm × 10 mm, 1.8 μm). As described previously,[49,105] the quantitation of bile acids utilized standard substances of 28 bile acids, and d_4-CDCA as internal standards.

Construction of hX4-expressing stable cell lines

The stable cell line expressing hX4 was generated as previously described.[52] In brief, hX4 was subcloned into the PiggyBac Transposon vector and co-transfected with the hyperactive PiggyBac transposase into the HEK293T cells using polyethyleneimine (PEI). hX4-expressing cells were selected and maintained in DMEM containing 10% fetal bovine serum (FBS), 1 μg/ mL puromycin, 100 U penicillin, and 100 μg/ mL streptomycin in a humidified atmosphere at 37°C containing 5% CO_2.

FLIPR-Ca^{2+} assay

HEK-293T cells stably expressing hX4 or its variants or other human MRGPRX receptors were seeded in 96-well plates at a density of 50,000 cells per well one day before the assay. The following day, the cells were loaded with Fluo-8 AM (AAT Bio) for 1 hr and washed with Hank's Buffer with Hepes. Where indicated, compounds were added to the wells at various concentrations, and the Fluo-8 signal was measured using the FLIPR TETRA system (Molecular Devices).

NanoLuc assay

The NanoLuc assay was performed as previously described.[52] In brief, the reporter cell lines stably expressing CRE-NanoLuc or FXRE-NanoLuc were transfected with TGR5 or FXR-RXR plasmids, respectively. The transfected cells were then seeded in 96-well plates at a density of 50,000 cells per well. The culture medium was replaced the next day, and compounds were added to the wells at various concentrations; 0.01% DMSO (v/v) was used as a negative control. The plates were incubated at 37°C in

5% CO_2 for 24 hr, after which a 10 μL aliquot of cell culture medium was removed from each well and combined with 40 μL of medium and 50 μL assay buffer (containing 20 μM coelenterazine); after 5 min, luminescence was measured using an EnVision plate reader (PerkinElmer).

β-arrestin recruitment assay

HEK293T cells were plated into 96-well plates at 20,000 cells per well and, the next day, co-transfected with the hX4-smBit and LgBit-β-arrestin plasmids. 24 hr after transfection, the growth medium was replaced with Opti-MEM, and Nano-Glo Live Cell Substrate (Promega) was added. The cells were then incubated for 30 min at room temperature, and compounds were added to the wells at various concentrations; luminescence was measured using an EnVision plate reader (PerkinElmer).

Culture and electroporation of rat DRG neurons

Rat DRG neurons were isolated and cultured as previously described.[52] In brief, rat DRG tissues were obtained, cut into pieces <1 mm, and then digested in an enzyme solution containing 5 mg/ mL dispase and 1 mg/ mL collagenase at 37°C for 1 hr. After trituration and centrifugation, the cells were washed in 15% (w/v) BSA, resuspended in DMEM/ F12 containing 10% FBS, plated on glass coverslips coated with poly-D-lysine and laminin, cultured in an incubator at 37°C, and used within 24 hours of plating. Rat DRG neurons were electroporated as follows. After washing the neurons in 15% BSA, the neurons were resuspended in DMEM/ F12 and electroporated using a P3 Primary Cell 4D-Nucleofector X Kit L (Lonza) by the manufacturer's instructions. After electroporation, the neurons were cultured for 72 hours before being used to allow the transgenes to express.

Calcium imaging

For Ca^{2+} imaging experiments, cells were loaded at 37C for 1 hr with 5 μM Fluo-8 AM (AAT Bio). Indicated compounds were added to the cells in a chamber containing a custom-made 8-channel perfusion valve control system, and fluorescence images were acquired using a Nikon A1 confocal microscope.

Immunostaining of DRG neurons

DRG neurons were prepared as described above. Briefly, cells were fixed in freshly prepared 4% PFA in PBS for 20 min at room temperature (RT) and then washed 3 times using PBS for 10 min each. Cells were then incubated in PBC containing 0.1% Triton X-100 and 20% horse serum for 1 hour at RT, followed by primary antibody incubating overnight at 4°C. After washing 3 times with PBS for 10 min each, cells were incubated with secondary antibody for 1 hour at RT before mounting under glass coverslips and Fluoromount-G.

Generation of hMRGPRX4 humanized rats

Using CRISPR/Cas9 technology, the nucleotide sequence corresponding to the 28th amino acid to the stop codon in exon 2 in the rat *MrgA* gene was replaced with the *hX4-3xFlag-P2A-iCre-WPRE-polyA* sequence. In addition, CRISPR/Cas9 technology was used to insert the *CAG-loxP-Frt-Stop-loxP-Frt-hX4-3xflag-iP2A-mScarlet-f-WPRE-polyA* sequence into the *ROSA26* locus. F1 offspring were genotyped by tail biopsy. hX4 humanized rats were generated by crossing *MrgA::hX4-Cre* rats with *Rosa26::loxp-STOP-loxp-hX4-3x flag-mScarlet* rats.

Behavioral studies

Scratching behavioral experiments have been widely used to study the mechanisms of pruritogens evoking itch.[65,106–108] Pruritogens with much higher concentrations than the EC_{50} in their receptors were intradermally injected into the nape of the neck of animal models. If the pruritogens can induce itch, the animal models will scratch toward the injection site. The experiments were performed as previously described.[109] In detail, behavioral tests concerning genotype and compounds used were performed and analyzed by an experimenter who was blind. Five days before the experiment, the animals were placed in the test chamber for 1 h daily. On the day of the investigation, the animals were first allowed to acclimatize to the test chamber, and basal scratching behavior was recorded for 60 min. Pruritic compounds were then injected intradermally into the nape of the neck or cheek (in a volume of 50 μl), and scratching behavior was recorded for 60 min. Scratching was defined as continuous scratching movement by the ipsilateral hind paw toward the injection site. Scratching behavior was quantified by counting the number of scratching bouts within the 30- or 60-minute observation period.

Human itch test

All subjects provided written informed consent and were provided with the experimental protocol. All injections were performed using the INJEX 30 needle-free injection system (Injex Pharma GmbH, Berlin, Germany). First, each test compound was dissolved to the final concentration in physiological saline containing 7% Tween-80 (Sigma-Aldrich). The injection site was cleaned with rubbing alcohol, and 25 μL of each solution was injected intradermally on the volar surface of both arms. The itch was defined as the desire to initiate scratching during the experiment. The subjects were instructed to rate the perceived intensity of the itch evoked by a given stimulus using the generalized labeled magnitude scale. For the anti-histamine pretreatment experiment, approximately 1.5 g of topical antihistamine cream (doxepin hydrochloride cream, Chongqing Huapont Pharm. Co., Chongqing, China) or a placebo

(cold cream, Eau Thermale Avène, Paris, France) was applied 2.5 hr before injection; any unabsorbed cream was removed with rubbing alcohol. OCA was prepared as described above; 25 μL of the OCA solution was injected into the volar surface of the arm as explained above. Each subject received two intradermal injections of OCA (one at the antihistamine-treated site and one at the placebo-treated site). The subjects were instructed to rate the itch sensation as described above.

Quantitative PCR

HepG2 cells purchased from ATCC were seeded in 6-well cell culture plates and cultured overnight. The following day, the culture medium was replaced with a serum-free medium, and indicated compounds were added to the wells. 24 hr later, cells were collected, and total RNA was extracted according to the manufacturer's instructions (Beyotime). For liver samples, tissues were immediately frozen in liquid nitrogen. About 50 mg tissues were mechanically homogenated with magnetic beads in a freezing grinder (JXFSTPRP-CL) in 1 mL Trizol. After centrifugation, the supernatant was used for RNA extraction according to the manufacturer's instructions (Beyotime). RNA samples were stored at -80 °C until used. After DNase-I treatment (Thermo) purification from genomic DNA, quantification and integrity analysis of total RNA (NanoDrop 5500, Thermo) were performed. To obtain the cDNA, 1 μg total RNA from each sample was reverse-transcribed using the BeyoRT first-strand cDNA synthesis kit (RNase H minus) (Beyotime) in a 20 μL reaction volume following the manufacturer's specifications. The mRNA expression levels of target genes were determined by the LightCycler® 96 system (Roche) with diluted cDNA products, primers, and AceQ qPCR SYBR Green Master Mix (Vazyme). The results are relative to GAPDH expression levels. Primers are provided in Table S2.

ANIT rat model

The Sprague-Dawley rats were randomly divided into several groups. One group received saline, and all other groups received two oral doses of ANIT (50 mg/kg dissolved in olive oil, two days apart) to induce intrahepatic cholestasis. Indicated compounds were dissolved in Veh (10% DMSO + 40% PEG + 10% Tween 80 + 40% saline) and given by oral gavage daily for four consecutive days. The rats were sacrificed at the end of the experiment, and blood and liver samples were taken for biochemical testing, RNA-seq, and pathology, respectively.

TAA rat model

The Sprague-Dawley rats were randomly divided into several groups. One group received saline, and all other groups received intraperitoneal injections of TAA (150 mg/kg, three times per week for eight weeks) to induce chronic liver injury and fibrosis. Veh or indicated compounds were given orally daily for five weeks at the end of the third week in the TAA-treatment rats. The rats were sacrificed at the end of the experiment, and blood and liver samples were taken for biochemical testing, RNA-seq, and pathology, respectively.

BDL mouse model

The C57BL/6J mice were randomly divided into two groups. BDL was performed in one group as described before,[110] and a sham operation was conducted in the other group. After healthy feeding for seven days, the mice in the BDL group were randomly divided into several groups, Veh or indicated compounds were given orally daily for seven days. The mice were sacrificed at the end of the experiment, and blood and liver samples were taken for biochemical testing and pathology, respectively.

HFD+CCl_4 mouse model

FOR TEN WEEKS, the C57BL/6J mice were fed either a standard-fat diet or HFD (D12492, Research Diets). The HFD-induced obese mice were then randomly divided into several groups based on the principle of minimum weight differences. In week 10, the HFD-fed mice received intraperitoneal injections of 25% CCl_4 in edible-grade olive or pure olive oil (2 mL/kg) twice weekly for four weeks. In week 10, the HFD-fed mice received daily oral doses of Veh or indicated compounds for four weeks. After four weeks, the mice were sacrificed at the end of the experiment, and blood and liver samples were taken for biochemical testing and pathology, respectively.

Transcriptomic analysis

KEGG pathway enrichment analysis and heatmap plot were performed using R script.

Biochemical analysis

After blood samples coagulation, serum was collected by centrifugation at 4000 g for 10 min (4°C) and then stored at -80°C. Serums were then diluted for measurement (50 μL serum + 150 μL saline). An automated clinical chemistry analyzer quantified the concentration of AST, ALT, ALP, TB, TG, TC, LDL-C, and HDL-C levels (Roche).

Histopathologic analysis

Portions of the liver lobes from each animal were fixed in 4% Paraformaldehyde Fix Solution. Liver sections were embedded in paraffin and then stained with H&E to visualize the patterns of necrosis, inflammation, and lipid accumulation. Collagen deposition (fibrosis) was observed by Sirius Red staining. Lipid droplet accumulation was observed by Oil Red staining. The histopathology images were captured and scanned with a light microscope (Olympus, Tokyo, Japan). We used QuPath80, a cell classifier, to quantify the liver injury index (numbers of necrosis and inflammatory cells/ numbers of total cells), collagen proportion area, and Oil Red

percentage (positive-staining areas/entire regions). NAS score consists of three components: steatosis (0–3), lobular inflammation (0–3), and hepatocyte ballooning (0–2).

QUANTIFICATION AND STATISTICAL ANALYSIS

Statistical analyses were performed using OriginPro 2020 and GraphPad prism 9.0. Group data were analyzed using students' t-tests, one-way ANOVAs, Mann-Whitney tests, or Wilcoxon matched-pairs signed-rank tests. *$p<0.05$; **$p<0.01$; ***$p<0.001$; and n.s., $p>0.05$.

Supplemental figures

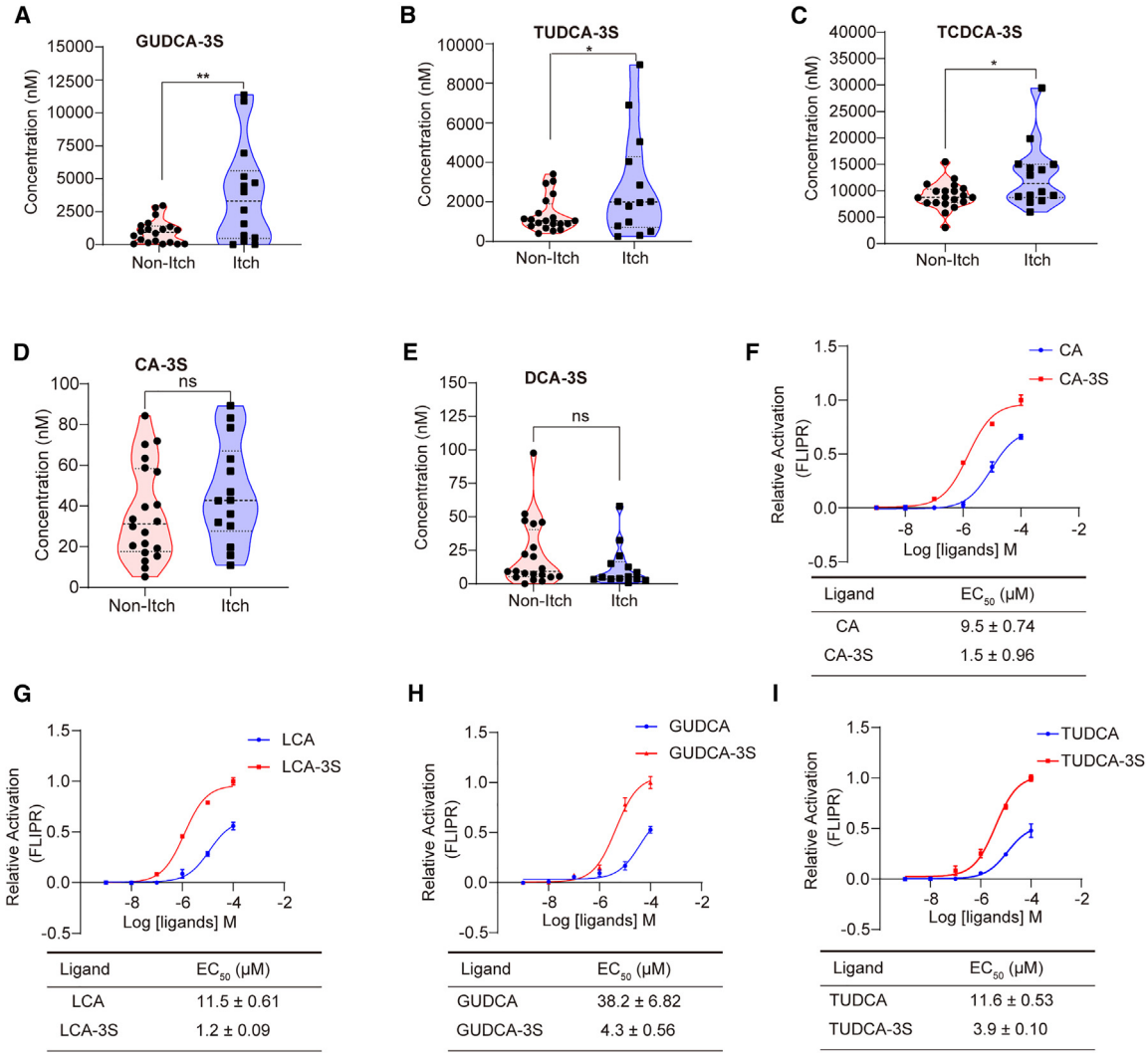

Ligand	EC_{50} (μM)
CA	9.5 ± 0.74
CA-3S	1.5 ± 0.96

Ligand	EC_{50} (μM)
LCA	11.5 ± 0.61
LCA-3S	1.2 ± 0.09

Ligand	EC_{50} (μM)
GUDCA	38.2 ± 6.82
GUDCA-3S	4.3 ± 0.56

Ligand	EC_{50} (μM)
TUDCA	11.6 ± 0.53
TUDCA-3S	3.9 ± 0.10

Figure S1. Bile acid profiling in cholestatic patients and the potency of different BAs in hX4, related to Figure 1

For all panels, $*p < 0.05$, $**p < 0.01$, $***p < 0.001$, and n.s., not significant ($p > 0.05$); paired two-way Student's t test (A, B, C, D, and E).

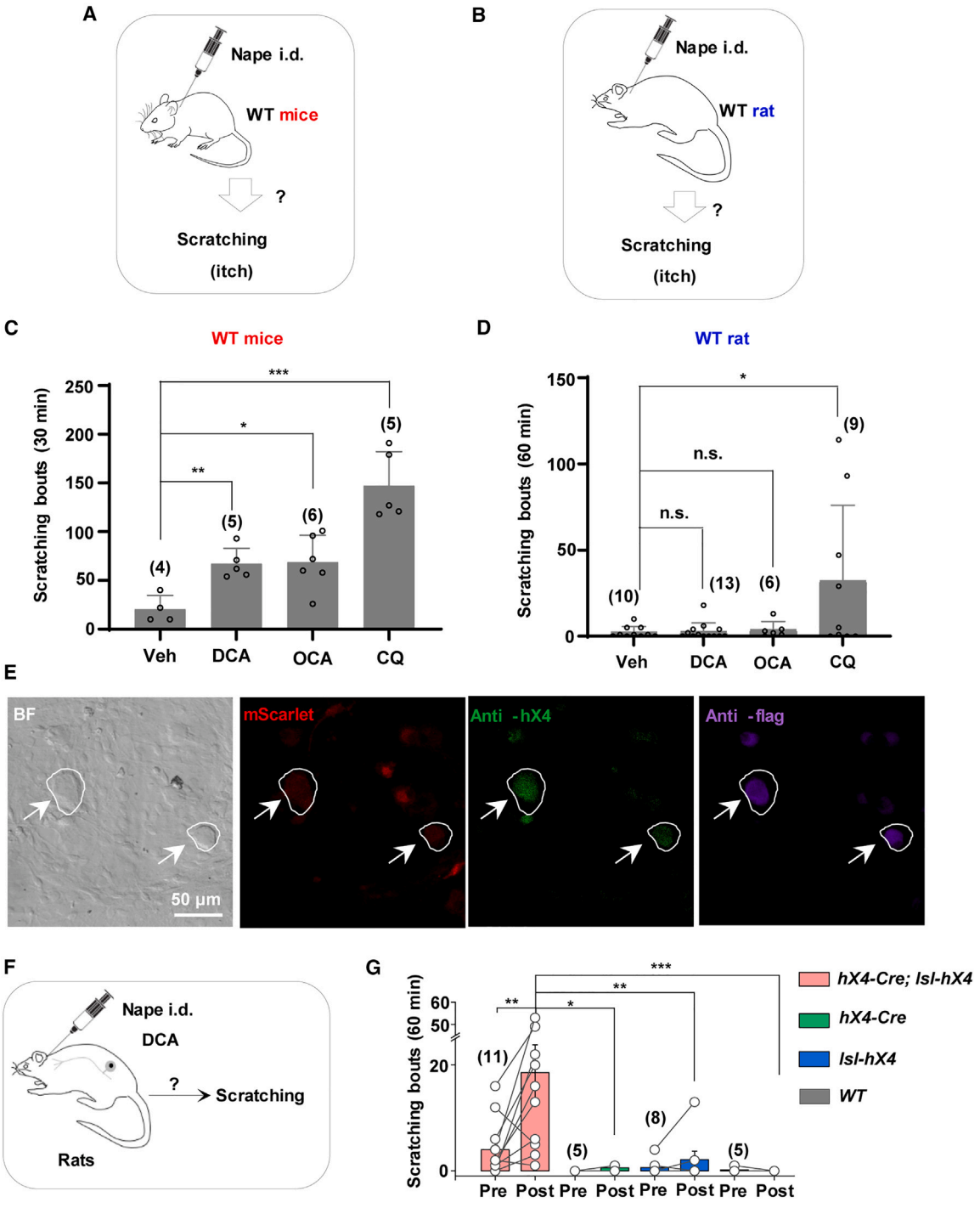

Figure S2. DCA and OCA induce significant scratching behavior in WT mice and hX4 humanized rats but not in WT rats, related to Figures 1 and 4

(A and B) The compounds of interest were intradermally (i.d.) into the nape of the neck of WT mice (A) and rats (B), respectively, spontaneous scratching over 30 min.

(C) Scratching bouts measured for 30 min in mice after i.d. injection of Veh, DCA (20 μg/50 μL), OCA (100 μg/50 μL), or chloroquine (CQ; 100 μg/50 μL). *n* = 4–6 per group.

(D) Scratching bouts measured for 60 min in rats after i.d. injection of Veh, DCA (500 μg/50 μL), OCA (300 μg/50 μL), or CQ (1 mg/50 μL). *n* = 6–13 per group.

(E) Representative images of cultured DRG neurons obtained from hX4-humanized rats. Arrows indicate DRG neurons expressing mScarlet and positive for both anti-hX4 and anti-flag immunofluorescence. Scale bar = 50 μm.

(legend continued on next page)

(F and G) DCA induces scratching behavior in hX4-humanized rats. Schematic diagram depicting the scratching behavior test (F). Scratching bouts were counted for 1 h prior to injection (Pre); after an i.d. injection of DCA (500 μg/ 50 μl) into the nape of the neck, scratching bouts were counted for 1 h (Post). Summary of the number of scratching bouts measured for 1 h before and after injection of DCA in indicated rats with different genotype (G). n = 5–11 per group.
For all panels, $^{*}p < 0.05$, $^{**}p < 0.01$, $^{***}p < 0.001$, and n.s., not significant ($p > 0.05$); unpaired two-way Student's t test.

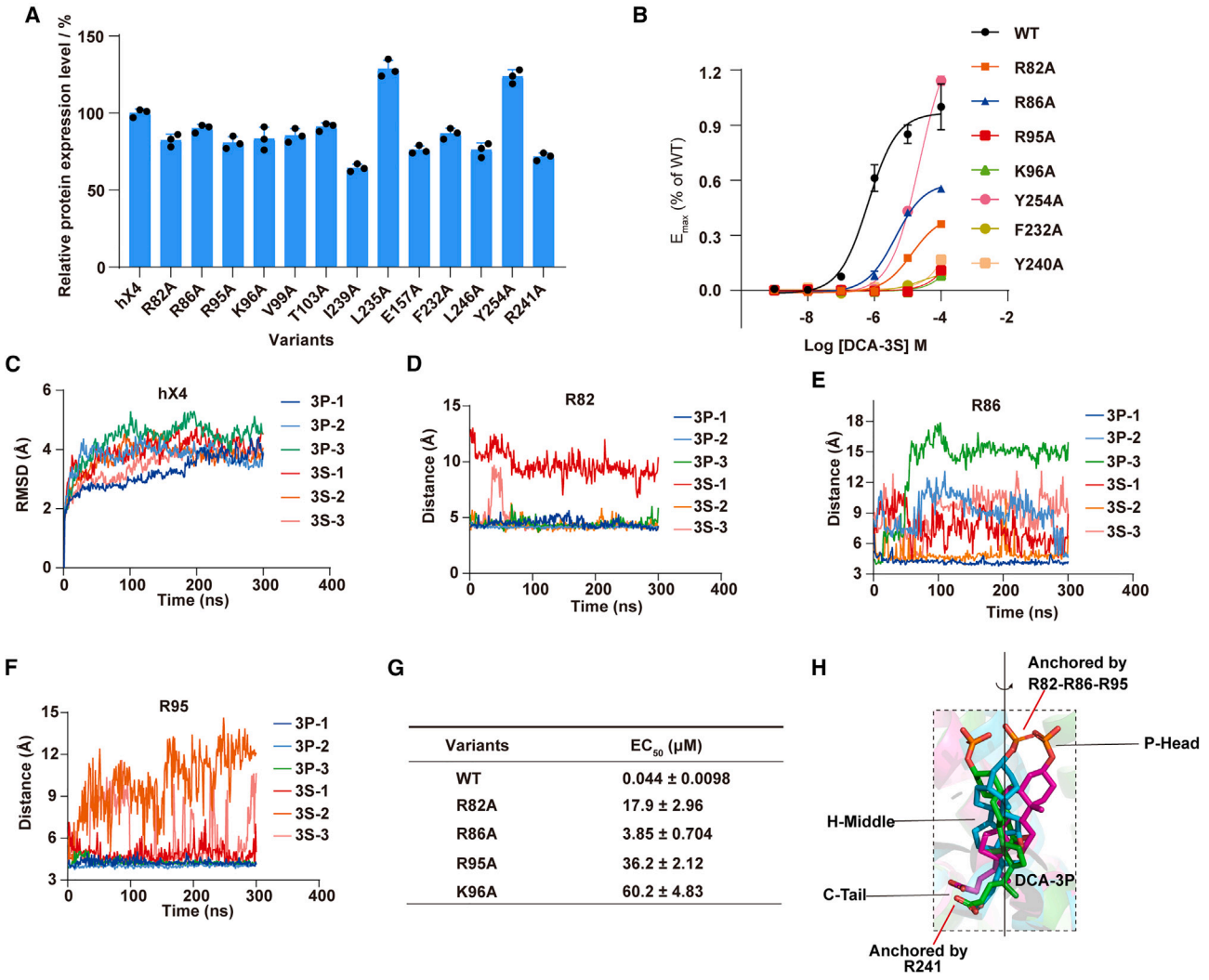

Variants	EC_{50} (μM)
WT	0.044 ± 0.0098
R82A	17.9 ± 2.96
R86A	3.85 ± 0.704
R95A	36.2 ± 2.12
K96A	60.2 ± 4.83

Figure S3. The activity of DCA-3S toward hX4's variants and MD simulations confirm the importance of R82, R86, and R95 for X4 recognition of DCA-3P and DCA-3S, related to Figure 3

(A) Protein expression level of hX4 variants in HEK293T cell lines.

(B) All the variants decrease their affinity for DCA-3S according to the FLIPR-Ca^{2+} assay.

(C) RMSD of X4 has no apparent fluctuation during 300 ns MDs.

(D–F) R82 (D), R86 (E), and R95 (F) form strong interactions with 3-sulfonate or 3-phosphate groups of DCA-3S or DCA-3P during MDs.

(G) EC_{50} of DCA-3P toward X4 variants R82A, R86A, and R95A determined by FLIPR-Ca^{2+} assay.

(H) P-head and C-tail were anchored by R82-R86-R95 and R241, respectively, while H-middle can rotate around the intermediate shaft during MDs.

For all panels, the data are means ± SEM of n = 3 biological replicates.

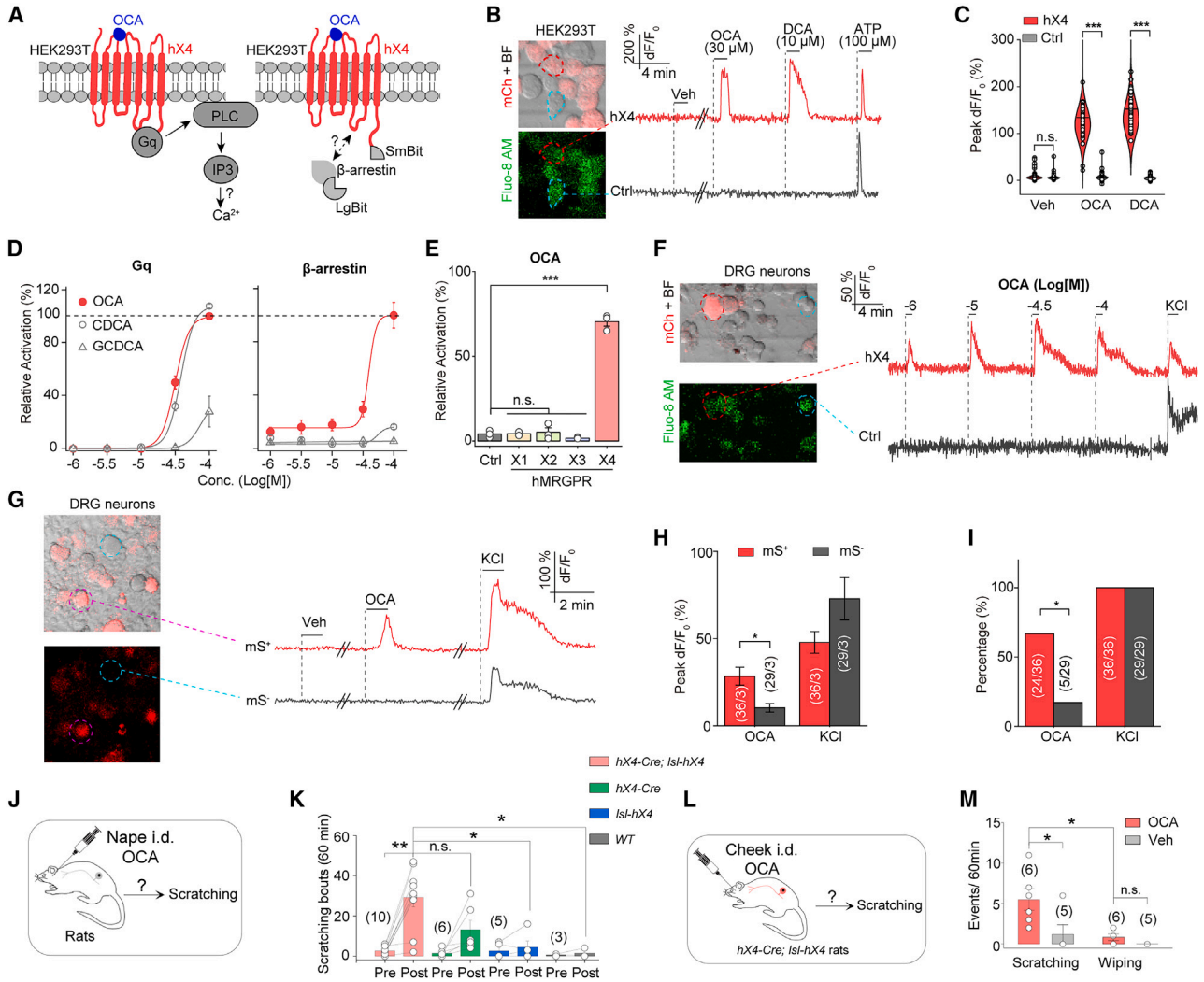

Figure S4. OCA can induce itch by activating hX4, related to Figure 4

(A) Schematic of the experimental rationale for measuring OCA-induced activation of hX4 using calcium imaging and the β-arrestin recruitment assay.

(B) OCA-induced activation of hX4 measured using calcium imaging. Left, representative images of HEK293T cells expressing hX4 (encircled by a red dashed line) and an hX4-negative neuron (Ctrl, surrounded by the cyan dashed line). The cells were loaded with the fluorescent Ca^{2+} indicator Fluo-8 AM: scale bar, 10 μm. Right, representative traces of the Fluo-8 AM signal measured in the neurons are shown on the left. Where indicated, OCA (30 μM), DCA (10 μM), and ATP (100 μM) were applied.

(C) The relative peak dF/F_0 measured in hX4 and Ctrl cells. n = 145–199 cells from 3 coverslips.

(D) Dose-response curve of hX4 activation in response to OCA, CDCA, and GCDCA measured using the FLIPR assay (left) or β-arrestin recruitment assay (right).

(E) OCA (30 μM)-induced signal in HEK293T cells or cells expressing human MRGPRX1, MRGPRX2, MRGPRX3, or MRGPRX4. Relative to ATP (300 μM), BAM 8–22 (10 μM), cortistatin-14 (10 μM), ATP (300 μM), or DCA (100 μM)-induced signal, respectively.

(F) OCA activates hX4 expressed in DRG neurons. Left, representative BF image of cultured rat DRG neurons transfected with hX4; an hX4-expressing neuron (hX4) and a control neuron (Ctrl) were encircled by white or cyan dashed line, respectively. Right, Representative traces of the Fluo-8 AM signal of hX4 and Ctrl neuron. Where indicated, OCA (1, 10, 30, and 100 μM) and KCl (65 mM) were applied.

(G–I) Representative traces (G), peak response (H), and percentage (I) of the Ca^{2+} signals measured in mS^+ neurons (red) and mS^- neurons (black) obtained from an *hX4-Cre; lsl-hX4* rat. Neurons having a response of $dF/F_0 > 10\%$ are defined as responsive. OCA (100 μM) and KCl (75 mM) were applied. n = 29–36 neurons from 3 coverslips.

(J and K) OCA (300 μg/50 μL) was injected intradermally into the nape of different rats, spontaneous scratching over 60 min (J). hX4 humanized rats (*hX4-Cre; lsl-hX4*) exhibited scratching behavior (K). n = 3–10 per group.

(L and M) OCA (300 μg/50 μL) was injected intradermally into the cheek of hX4 humanized rats; spontaneous scratching and wiping events were counted for 60 min (L). OCA induces significant scratching, but not wiping behavior, in hMRGPRX4 humanized rats (M). n = 5–6 per group.

For all panels, $^*p < 0.05$, $^{**}p < 0.01$, $^{***}p < 0.001$, and n.s. = not significant ($p > 0.05$); unpaired two-way Student's t test (C, E, and H); two-proportion z-test (I); Kruskal-Wallis ANOVA (K and M).

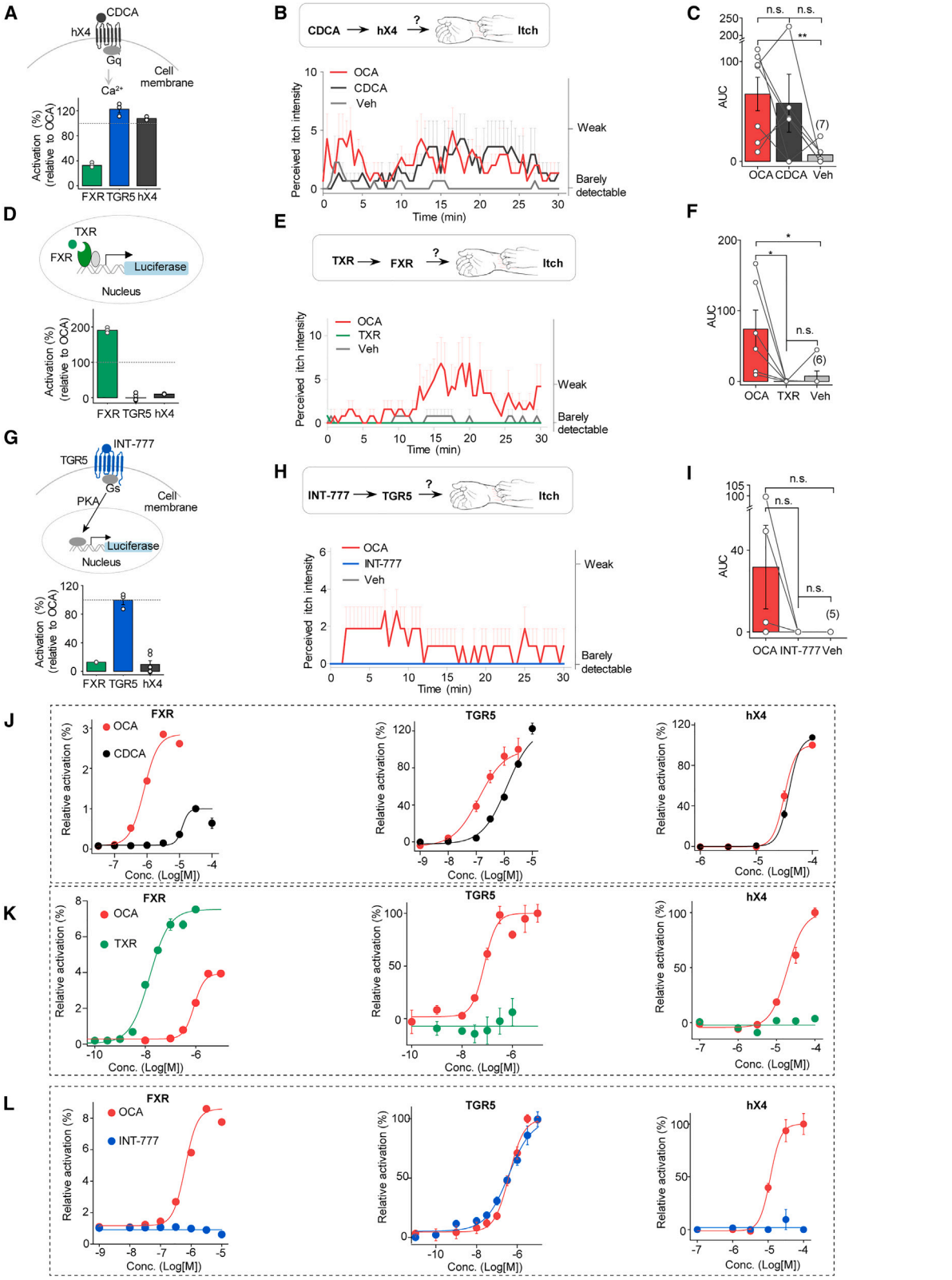

(legend on next page)

Figure S5. OCA directly evokes itch by activating hX4 but not FXR or TGR5, related to Figure 4

(A–C) Activation of hX4 induces itch in human subjects. On top is a schematic diagram depicting the *in vitro* assay used to detect activation of hX4. CDCA activates hX4 to cause an increase in intracellular Ca^{2+}. Bottom, maximal activation of human FXR (green), TGR5 (blue), and hX4 (black) by CDCA, normalized by the corresponding OCA-induced signal (A). Time course of perceived itch intensity evoked by OCA (100 μg in 25 μL), CDCA (100 μg in 25 μL), and Veh (25 μL) ($n = 7$). The equivalent concentration of CDCA is the same as that of OCA (B). The AUC of the itch intensity traces (C).

(D–F) Activation of FXR does not induce itch in human subjects. Top, an *in vitro* assay was used to detect activation of human FXR. TXR activates FXR to drive the expression of the downstream reporter gene luciferase. TXR, tropifexor. Bottom, maximal activation of human FXR (green), TGR5 (blue), and hX4 (black) by TXR normalized to the corresponding OCA-induced maximal signal (D). Time course of perceived itch intensity evoked in response to i.d. injection of OCA (200 μg in 25 μL), TXR (5 μg in 25 μL), or Veh (25 μL) ($n = 6$). The equivalent concentration means the fold of concentration used in the behavioral tests to the EC_{50} of activating human FXR. The equivalent concentration of TXR is 1.2-fold that of OCA (E). The AUC of the itch intensity traces (F).

(G–I) Activation of human TGR5 does not induce itch in human subjects. On top is a schematic diagram depicting the *in vitro* assay used to detect the activation of human TGR5. INT-777 activates TGR5 to drive the expression of the downstream reporter gene luciferase. Bottom, maximal activation of human FXR (green), TGR5 (blue), and hX4 (black) by INT-777 normalized to the corresponding OCA-induced maximal signal (G). Time course of perceived itch intensity in response to OCA (50 μg in 25 μL), INT-777 (50 μg in 25 μL), and Veh (25 μL) ($n = 5$). The equivalent concentration of INT-777 is the same as that of OCA (H). The AUC of the itch intensity traces (I).

(J) Dose-response curves of FXR, TGR5, and hX4 activation in response to OCA and CDCA.

(K) Dose-response curves of FXR (relative to CDCA (30 μM)-induced signal), TGR5 (relative to forskolin (10 μM)-induced signal), and hX4 (relative to DCA (100 μM)-induced signal) activation in response to OCA and TXR.

(L) Dose-response curves of FXR, TGR5, and hX4 activation in response to OCA and INT-777.

For all panels, $^{*}p < 0.05$, $^{**}p < 0.01$, $^{***}p < 0.001$, and n.s., not significant ($p > 0.05$); paired two-way Student's t test.

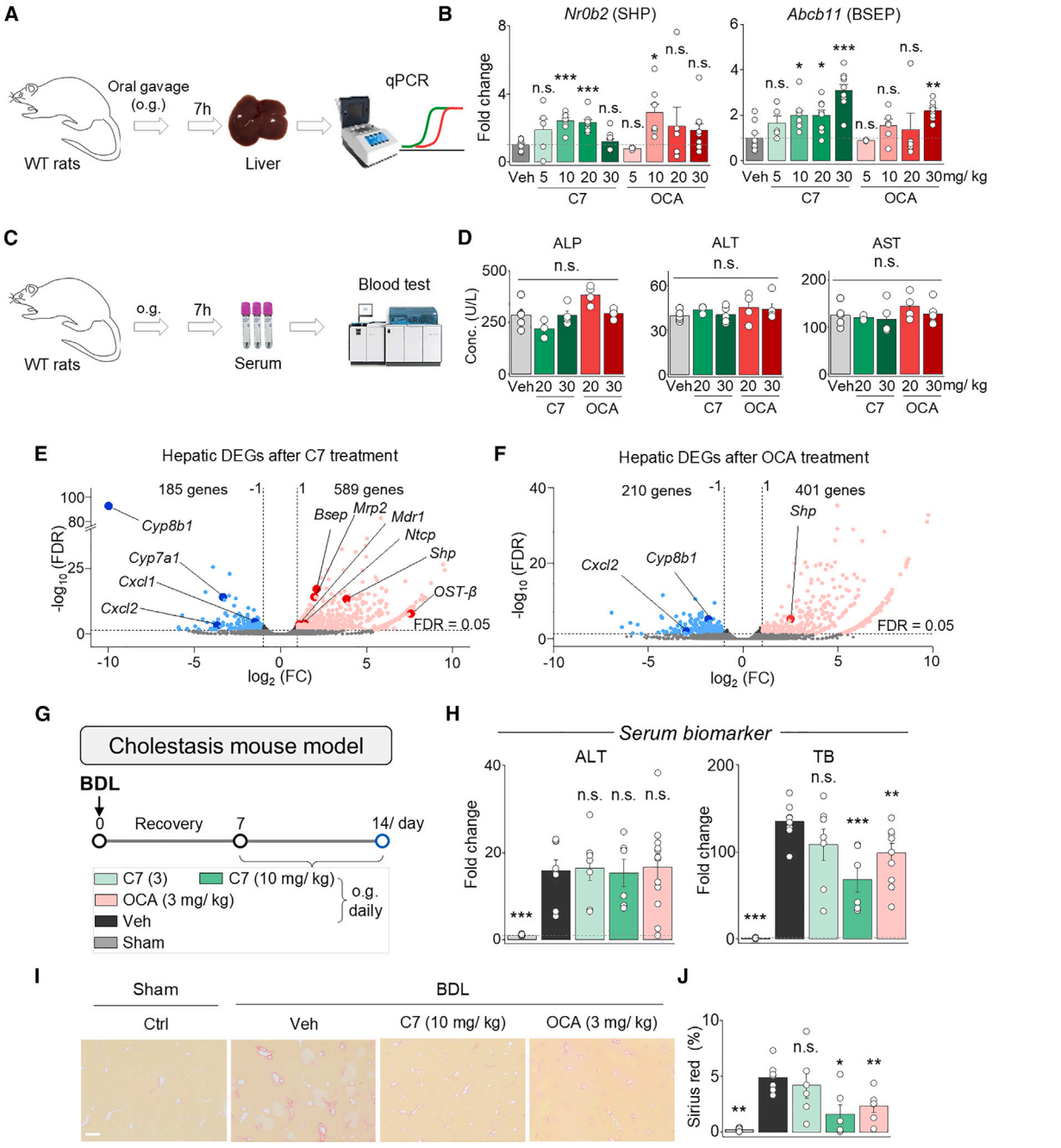

Figure S6. C7 regulates the expression of genes downstream of FXR and ameliorates liver injury in cholestasis, related to Figures 6 and 7

(A and B) C7 regulates downstream gene expression in WT rats. Seven hours after receiving a single oral dose of vehicle (Veh), C7, or OCA, the liver samples were collected and used to measure mRNA levels using qPCR (A). Relative expression levels of Nr0b2 and Abcb11 mRNA following an oral dose of Veh, C7, or OCA at the indicated doses (B). *n* = 5–10 per group.

(C and D) C7 does not significantly increase serum transaminase levels. Seven hours after receiving a single oral dose of Veh, C7, or OCA, serum was collected and used to measure serum transaminase levels (C). Serum alkaline phosphatase (ALP), alanine transaminase (ALT), and aspartate transaminase (AST) levels following an oral dose of Veh, C7, or OCA at the indicated doses (D). *n* = 5–10 per group.

(E and F) Volcano plots showing the distribution of all differentially expressed genes (DEGs; red and blue indicate significantly upregulated and downregulated genes, respectively) in ANIT-treated rats following administration of 10 mg/kg C7 (E) or OCA (F). The vertical dashed lines indicate −1 and 1, corresponding to a 2-FC in expression, and the horizontal dashed line indicates a false discovery rate (FDR, adjusted *p* value) of 0.05. FC, fold change.

(G) C57BL/6J mice were subjected to BDL to induce extrahepatic cholestasis; Ctrl mice were sham-operated. After 1 week of recovery, the mice received daily oral gavage (o.g.) of C7 (3 or 10 mg/kg), OCA (3 mg/kg), or Veh for 7 days. The Ctrl mice were sham-operated and given Veh.

(legend continued on next page)

(H) Fold change in serum ALT and TB levels, expressed relative to the Ctrl group. $n = 6–12$.
(I) Sirius red-stained liver sections prepared from the mice in the indicated groups: scale bar, 200 μm.
(J) The liver fibrosis area measured in the indicated groups is shown in c and expressed relative to the Veh group. $n = 4–7$.
For all panels, $^{*}p < 0.05$, $^{**}p < 0.01$, $^{***}p < 0.001$, and n.s. = not significant ($p > 0.05$) versus the corresponding Veh group (one-way ANOVA).

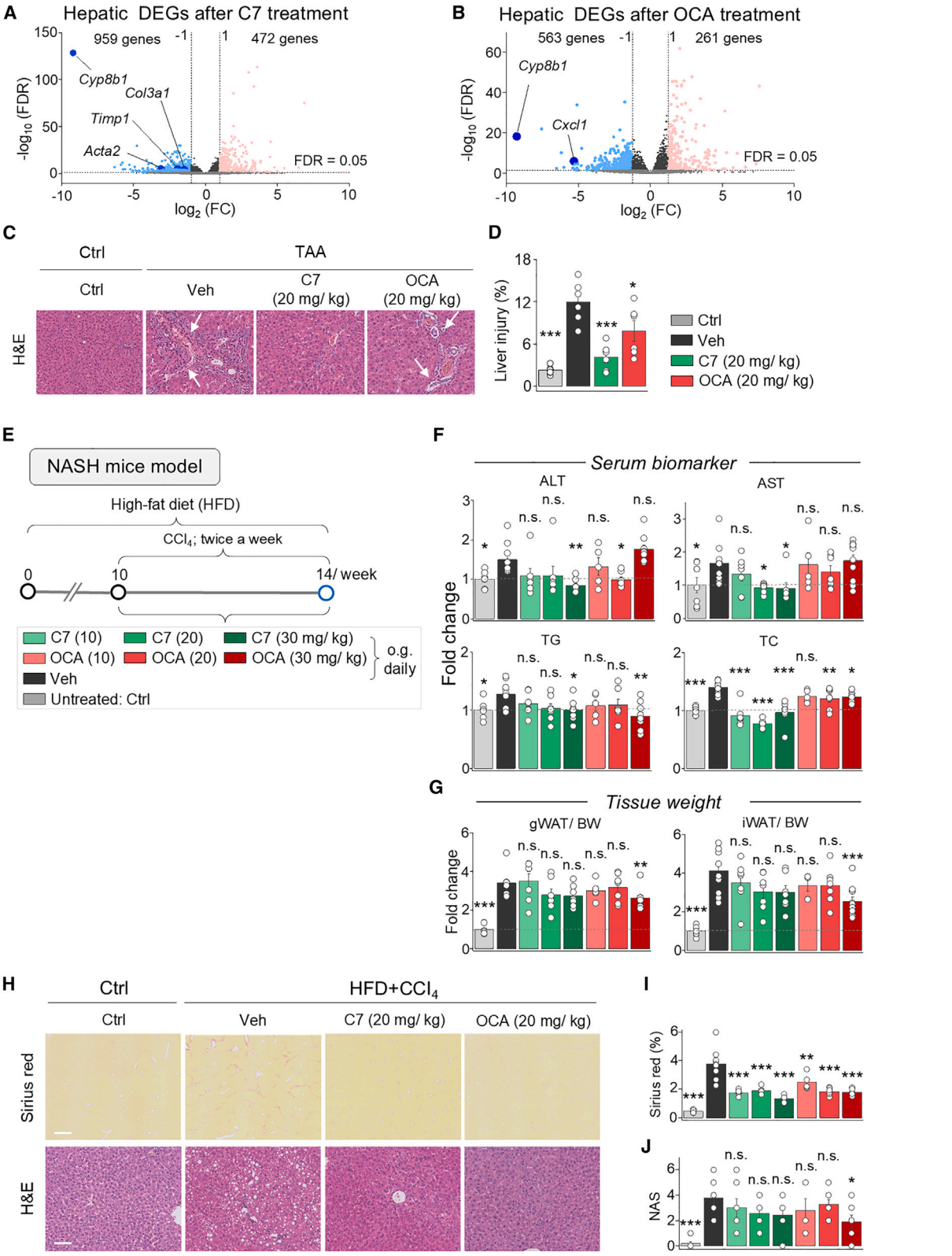

(legend on next page)

Figure S7. C7 reduces liver injury and fibrosis in TAA-induced NASH rat and mouse models, related to Figure 7

(A and B) Volcano plot showing the distribution of hepatic DEGs (red and blue represent significantly upregulated and downregulated genes, respectively) in TAA-treated rats following administration of 20 mg/kg C7 (A) or OCA (B). The vertical dashed lines indicate -1 and 1, corresponding to a 2-FC in expression, and the horizontal dashed line represents an FDR of 0.05.

(C) H&E-stained liver sections from the rats in the indicated groups. Arrows indicate hepatocyte damage and immune cell infiltration: scale bars, 50 μm.

(D) Quantification of liver injury measured as shown in (C). $n = 6$.

(E) C57BL/6J mice were fed a high-fat diet (HFD) for 14 weeks; starting at week 10, the mice received CCl4 twice a week together with daily doses of C7 (10, 20, or 30 mg/kg), OCA (10, 20, or 30 mg/kg), or Veh. The Ctrl mice were untreated healthy mice.

(F) Fold change in serum ALT, AST, TG, and TC concentrations, expressed relative to the Ctrl group. $n = 5–6$ per group.

(G) Fold change in the ratio between visceral-gonadal white adipose tissue (gWAT) and body weight (left) and between inguinal white adipose tissue (iWAT) and body weight (right), expressed relative to the Ctrl group. $n = 5–10$ per group.

(H) Sirius red-stained liver sections (top row) and H&E-stained liver sections (bottom row) from the mice in the indicated groups: scale bars, 100 μm.

(I) The Sirius red-stained area was quantified as shown in (H). $n = 5–9$ per group.

(J) Quantifying the histological NAFLD activity score (NAS) measured in the indicated group, as shown in (H). $n = 5–9$ per group.

$^{*}p < 0.05$, $^{**}p < 0.01$, $^{***}p < 0.001$, and n.s. = not significant ($p > 0.05$) versus the corresponding Veh group (one-way ANOVA).